A Tropical Stochastic Skeleton Model for the MJO, El Niño and Dynamic Walker Circulation: A Simplified GCM

Sulian Thual [(1)], Andrew J. Majda [(1,2)], and Nan Chen[(1)]

(1) Department of Mathematics, and Center for Atmosphere Ocean Science, Courant Institute of Mathematical Sciences, New York University, 251 Mercer Street, New York, NY 10012 USA

(2) Center for Prototype Climate Modeling, New York University Abu Dhabi, Saadiyat Island, Abu Dhabi, UAE

Corresponding author:

Nan Chen, 251 Mercer Street, New York, NY 10012 USA, *nan.chen@nyu.edu*

submitted to Journal of Climate

Abstract

A simple dynamical stochastic model for the tropical ocean-atmosphere is proposed that captures qualitatively major intraseasonal to interannual processes altogether including the El Niño Southern Oscillation (ENSO), the Madden-Julian Oscillation (MJO), the associated wind bursts and the background dynamic Walker circulation. Such a model serves as a prototype "skeleton" for General Circulation Models (GCMs) that solve similar dynamical interactions across several spatio-temporal scales but usually show common and systematic biases in representing tropical variability as a whole. The most salient features of the ENSO, the wind bursts and the MJO are captured altogether including their overall structure, evolution and energy distribution across scales, in addition to their intermittency and diversity as well as their fundamental interactions. Importantly, the intraseasonal wind bursts and the MJO are here solved dynamically which provides their upscale contribution to the interannual flow as well as their modulation in return in a more explicit way. This includes a realistic onset of El Niño events with increased wind bursts and MJO activity starting in the Indian ocean to western Pacific and expanding eastward towards the central Pacific, as well as significant interannual modulation of the characteristics of intraseasonal variability. A hierarchy of cruder model versions is also analyzed in order to highlight fundamental concepts related to the treatment of multiple time scales, main convective nonlinearities and the associated stochastic parameterizations. The model developed here also should be useful to diagnose, analyze and help eliminate the strong tropical biases which exist in current operational models.

1 Introduction

The El Niño-Southern Oscillation (ENSO) is the dominant global climate signal on interannual time scales, with dramatic worldwide ecological and social impacts. It consists of alternating periods of anomalously warm El Niño conditions and cold La Niña conditions every 2 to 7 years, with considerable irregularity in amplitude, duration, temporal evolution and spatial structure of these events. Its dynamics in the equatorial Pacific result largely from coupled interactions between the ocean and atmosphere at interannual timescale and planetary scale (Neelin et al., 1998; Clarke, 2008). One salient yet not fully understood feature of the ENSO is its interaction with atmospheric processes on a vast range of spatio-temporal scales. For instance, a broad range of intraseasonal atmospheric disturbances in the tropics may be considered as possible triggers to El Niño or La Niña events (Kleeman, 2008). Those atmospheric disturbances are usually generally denoted as westerly wind bursts (WWB) or easterly wind bursts (EWBs) though they may have different origins such as tropical cyclones, mid-latitude cold surges as well as the convective envelope of the Madden-Julian Oscillation (MJO), among others (Harrison and Vecchi, 1997; Vecchi and Harrison, 2000; Kiladis et al., 2009). In particular, westerly wind bursts reach strong intensity levels over the western Pacific warm pool during the onset of El Niño events (Tziperman and Yu., 2007). The MJO is the dominant component of intraseasonal variability in the tropics and plays an important role for the generation of wind bursts (Madden and Julian, 1971; Madden and Julian, 1994). In the troposphere, it begins as a standing wave in the Indian Ocean and propagates eastward as an equatorial planetary-scale wave across the western Pacific ocean at a speed of around $5\,ms^{-1}$ (Zhang, 2005). The MJO features both westerly and easterly wind bursts at the same time within its convective envelope (Puy et al., 2016), and is also more prominent during the onset of El Niño events (Kleeman and Moore, 1997; Moore and Kleeman, 1999; Zhang and Gottschalck, 2002; McPhaden et al., 2006; Hendon et al., 2007). In addition to the above features, the ENSO dynamics are also closely linked to the destabilization of the background equilibrium circulation in the equatorial Pacific, the so-called Walker circulation that consists of an overturning zonal-vertical atmospheric circulation along with a zonal sea-saw gradient of sea surface temperatures and thermocline depth in the ocean (Clarke, 2008).

The interaction between the ENSO, the wind bursts and the Walker circulation is the focus of various observational initiatives and modeling studies. The challenges to deal with are two-fold. First, General Circulation Models (GCMs) have common and systematic biases in representing the ENSO, the intraseasonal atmospheric variability and the background circulation in the tropics altogether (Lin et al., 2006; Kim et al., 2009; Wittenberg et al., 2004; 2006; 2014; Guilyardi et al., 2016). In these models computing resources are significantly limited. For example, the spatial resolution is only up to $\approx 10-100\,km$, and therefore several important small scales are unresolved or parameterized according to various recipes. As regards tropical convection, unresolved processes at smaller scales such as deep convective clouds show some particular features in space and time, such as high irregularity, high intermittency and low predictability. Recent improvements suggest that suitable stochastic parameterizations are good candidates to account for those processes while remaining computationally efficient (Majda et al., 2008; Palmer, 2012; Weisheimer et al., 2014; Deng et al., 2014; Goswami et al., 2016; 2017; Christensen et al., 2017). Second, there is a general lack of theoretical understanding of the dynamical interactions between the ENSO and the wind bursts in GCMs. On the other hand, insight has been gained from intermediate and simple models which have more tractable dynamics, are more computationally efficient and allow for more detailed and systematic statistical analysis (e.g. Moore and Kleeman, 1999; Neelin and Zeng, 2000; Zeng et al., 2000; Jin et al., 2007; Gushchina and Dewitte, 2011; Chen et al., 2015; Thual et al., 2016). For example, those models indicate the multiplicative noise features that can exist when wind bursts depend on the state of the equatorial Pacific system (Eisenman et al., 2005; Tziperman and Yu., 2007; Gebbie et al., 2007; Lopez et al., 2013). Yet, in those models wind bursts are usually not resolved dynamically but are described by simple stochastic parameterizations that prescribe the wind burst amplitudes, durations and/or propagation. As a result, those simple models do not resolve some of the important wind bursts details such as their dynamical evolution and origins.

In the present article, a simplified dynamical stochastic model is developed for the intraseasonal to interannual variability in the tropics and background circulation. The model is denoted hereafter "Tropical Stochastic Skeleton Model GCM" (TSS-GCM). The present model serves as a prototype "skeleton" for General Circulation Models (GCMs) that solve similar dynamical interactions across several spatio-temporal scales. As compared to conventional GCMs the present TSS-GCM model includes simple tractable dynamics with a minimal number of processes and parameters, and is computationally very uncostly. Importantly, while conventional GCMs have common and systematic biases in representing tropical variability as a whole, the TSS-GCM model succeeds in capturing major intraseasonal to interannual processes as well as their fundamental interactions in qualitative fashion. First, at intraseasonal timescales, the TSS-GCM model captures dynamical wind bursts with realistic intermittency, localization, lifespan, convective features, energy distribution across scales and generation from various sources including from the MJO. In particular, the main features of the MJO are recovered including its eastward propagation, structure and organization into intermittent wavetrains with growth and demise. Second, at interannual timescales, the TSS-GCM model captures the overall structure and period of the ENSO, in addition to its intermittency and diversity with El Niño events of varying strength and intensity. The associated dynamic background Walker circulation is also captured qualitatively. Third and most important, the TSS-GCM model captures the most salient interactions between the ENSO, wind bursts and the MJO. This includes a realistic onset of El Niño events with increased wind bursts and MJO activity starting in the Indian to western Pacific ocean and expanding eastward towards the central Pacific. In return, the characteristics of wind bursts and the MJO are significantly modulated interannually by the underlying variations of sea surface temperatures associated with the ENSO, as in nature. The TSS-GCM model formulation provides such an upscale contribution of the wind bursts to the interannual flow and their modulation in return in an explicit and dynamical way.

The TSS-GCM model introduced in the present article captures in simple fashion the ocean and atmosphere dynamics in the tropics ranging from intraseasonal to interannual time scale and builds on a range of previous work by the authors. First, for the intraseasonal variability in the atmosphere Majda and Stechmann (2009; 2011) introduced a minimal dynamical model, the skeleton model, that captures for the first time the main features of the MJO. This includes the MJO eastward phase speed of $5\,m.s^{-1}$, peculiar dispersion relation with $d\omega/dk \approx 0$ and horizontal quadrupole structure, among others. The model depicts the MJO as a neutrally-stable atmospheric wave that involves a simple interaction between planetary-scale, dry dynamics, planetary-scale, lower-tropospheric moisture and the planetary envelope of synoptic-scale convection/wave activity. In subsequent work, such a MJO skeleton model refined with a suitable stochastic convective parameterization has been shown to capture the intermittent generation of MJO events and their organization into waves trains with growth and demise (i.e. series of consecutive events), as in nature (Thual et al., 2014; Stachnik et al., 2015; Majda et al., 2018). The MJO skeleton model appears to be an excellent candidate for capturing dynamically the variability of intraseasonal wind bursts in simple fashion. In the present TSS-GCM model, such a skeleton atmosphere with simple self consistent nonlinear noise (Chen and Majda, 2016a) is used with a simple multiple time approach (Majda and Klein, 2003) that allows us to derive approximate dynamics on both the intraseasonal and interannual timescale. Second, for the interannual variability in general a simple ocean-atmosphere model was developed recently that emphasizes the role of state-dependent wind bursts and realistically captures the ENSO diversity including the eastern Pacific moderate and occasional super El Niño (Thual et al., 2016). In this coupled model stochastic wind bursts are coupled to otherwise deterministic, linear and stable ocean-atmosphere dynamics: in fact, the wind bursts play the role of maintaining the ENSO, which is fundamentally different from the Cane-Zebiak (Zebiak and Cane, 1987) and other nonlinear models that rely instead on internal instability. In subsequent work such a simple model has been refined in order to facilitate additional realistic features such as the occurrence of central Pacific El Niño events (Chen and Majda, 2016b; 2017; Chen et al., 2018) as well as the synchronization of the ENSO to the seasonal cycle (Thual et al., 2017). However, such a coupled model does not solve wind bursts dynamically: instead it uses a simple stochastic parameterization to generate randomly both WWBs and EWBs from an identical white noise source the intensity of which depends on the strength of the western Pacific warm pool. In the TSS-GCM model from the present article, such coupled ocean-atmosphere dynamics from Thual et al. (2016) are included with a more realistic depiction of wind bursts and their dynamical features directly from the coupled atmosphere skeleton model.

The present article is organized as follows. In Section 2 we present the TSS-GCM model used in this study, along with a hierarchy of cruder versions of the model used to introduce progressively fundamental concepts related to the treatment of multiple time scales, main convective nonlinearities and associated stochastic parameterizations. In Section 3 we analyze the main properties of the TSS-GCM model and its versions, including their depiction of the intraseasonal wind bursts and MJO variability, interannual ENSO variability as well as the dynamic Walker circulation. Section 4 is a discussion with concluding remarks.

2 Formulation of the Tropical Stochastic Skeleton GCM Model

In this section we formulate the TSS-GCM model used in the present study. Such a model captures in simple fashion the ocean and atmosphere processes in the tropics ranging from intraseasonal to interannual scale. In order to formulate the model, first, a starting deterministic atmosphere and ocean are considered (Majda and Stechmann, 2009; Thual et al., 2016; Chen and Majda, 2016b; 2017; Chen et al., 2018). In particular, the deterministic atmosphere is decomposed into an intraseasonal and interannual flow following a simple multiple time approach (Majda and Klein, 2003). Next, simplified versions of the TSS-GCM model are derived: a crude interannual model and crude intraseasonal model. Such cruder model versions differ from the complete TSS-GCM model by their simplified representations of intraseasonal processes, and are introduced first for dynamical insight. Finally, the complete TSS-GCM model is formulated as well as a more complete version with a dynamic Walker circulation. At the end of the section, an overview and intercomparison of the features of each model version is provided, as well as their contrast with conventional GCMs.

2.1 Starting Deterministic Atmosphere

In order to derive the TSS-GCM model, we consider first the starting deterministic skeleton model atmosphere from Majda and Stechmann (2009). Such a skeleton model captures the main features of intraseasonal variability in general in the tropics, including importantly the MJO eastward propagation, peculiar dispersion relation and quadrupole structure, among others (Majda and Stechmann, 2009; 2011). Such a model reads:

Starting deterministic atmosphere

$$\begin{aligned}
&\partial_t u - yv - \partial_x \theta = 0 \\
&yu - \partial_y \theta = 0 \\
&\partial_t \theta - (\partial_x u + \partial_y v) = \overline{H} a - s^\theta \\
&\partial_t q + \overline{Q}(\partial_x u + \partial_y v) = -\overline{H} a + s^q + E_q \\
&\partial_t a = \Gamma q a
\end{aligned} \tag{1}$$

In the above model, x is zonal direction, y is meridional direction and t is intraseasonal time. The u, v are zonal and meridional winds, θ is potential temperature, q is lower lever moisture and a is the planetary envelope of convective activity. All variables are anomalies except $a > 0$. The a in particular is a collective (i.e. integrated) representation of the unresolved convection/wave activity details occurring at synoptic-scale, always acting as a planetary source of heating and drying (hence $a > 0$). A key idea in the above model is that environmental moisture (q) influences the growth/decay of convective activity in general as well as their planetary envelope (a). Note that as compared to Majda and Stechmann (2009), we have added in Eq. 1 the contribution of latent heating E_q in order to allow coupling with the ocean. The s^θ, s^q are constant external sources of cooling and moistening, respectively, and $\overline{Q}$, Γ are parameters.

Next, the above system is decomposed into an intraseasonal atmosphere and interannual background mean atmosphere. A general motivation for this is to derive approximate solutions for the slowly varying fluctuations relevant to the ENSO. For this, we assume that such slowly varying fluctuations exist on the interannual time, in addition to the rapidly varying fluctuations on the intraseasonal time scale (Majda and Klein, 2003). Details on the derivation are provided in the appendix section A. The flow in Eq. 1 is decomposed as $a = \overline{a} + a'$ in standard notations from turbulence theory and similarly for u, v, θ, q. First, the resulting intraseasonal atmosphere reads:

Intraseasonal deterministic atmosphere

$$\begin{aligned} &\partial_t u' - yv' - \partial_x \theta' = 0 \\ &yu' - \partial_y \theta' = 0 \\ &\partial_t \theta' - (\partial_x u' + \partial_y v') = \overline{H} a' \\ &\partial_t q' + \overline{Q}(\partial_x u' + \partial_y v') = -\overline{H} a' \\ &\partial_t a' = \Gamma q' (\overline{a} + a'). \end{aligned} \tag{2}$$

which models intraseasonal fluctuations in general such as the MJO as well as other planetary convectively coupled waves. Such a system is dynamically similar to the starting skeleton model from Majda and Stechmann (2009; 2011), though the background $\overline{a}$ here varies interannually as modulated by the ocean conditions (with $\overline{a} \geq 0$, see hereafter). Note that the intraseasonal contribution of latent heat release E_q' is lower order and omitted here. Next, the interannual atmosphere reads:

Interannual deterministic atmosphere

$$\begin{aligned} &-y\overline{v} - \partial_x \overline{\theta} = 0 \\ &y\overline{u} - \partial_y \overline{\theta} = 0 \\ &-(\partial_x \overline{u} + \partial_y \overline{v}) = \overline{H}\overline{a} - s^\theta \\ &-\overline{Q}(\partial_x \overline{u} + \partial_y \overline{v}) = \overline{H}\overline{a} + s^q + E_q \\ &\overline{H}\overline{a} = (E_q + s^q - \overline{Q} s^\theta)/(1 - \overline{Q}) \end{aligned} \tag{3}$$

which depicts the interannual adjustment of the atmosphere to the ocean conditions. In particular, there are no time derivatives in the system from Eq. 3 that is assumed to remain in balance with the underlying ocean on the slow interannual time scale where the forcing E_q is assumed to vary (Gill, 1980). Such an interannual atmosphere is identical to the one from Thual et al. (2016), though it is derived here from a different method (multiple time scales instead of single time scale approach, see appendix section A). Note that wind divergence in Eq. 3 can alternatively be expressed as:

$$-(\partial_x \overline{u} + \partial_y \overline{v}) = (E_q + s^q - s^\theta)/(1 - \overline{Q}). \tag{4}$$

For instance, unbalanced sources of heating/moistening $(E_q + s^q - s^\theta) \neq 0$ force a background interannual circulation similar to the Walker circulation in nature (Chen and Majda, 2016b; Ogrosky and Stechmann, 2015), as discussed hereafter.

2.2 Starting Ocean, SST and Couplings

Next, the above deterministic atmosphere (Eq. 2 and Eq. 3) is coupled to the ocean. For this, we consider a simple shallow water ocean and Sea Surface temperature (SST) budget that retain a few essential processes relevant to the ENSO interannual variability. Because the ocean dynamics are essentially interannual, no multiple time approach is considered here. The starting ocean, SST budget, and couplings are identical to the ones of Thual et al. (2016). They read:

Ocean

$$\begin{aligned}
&\partial_t U - \epsilon c_1 Y V + \epsilon c_1 \partial_x H = \epsilon c_1 \tau_x \\
&Y U + \partial_Y H = 0 \\
&\partial_t H + \epsilon c_1 (\partial_x U + \partial_Y V) = 0
\end{aligned} \tag{5}$$

SST

$$\partial_t T = -\epsilon c_1 \zeta E_q + \epsilon c_1 \eta H \tag{6}$$

Couplings

$$\begin{aligned}
&\tau_x = \gamma(\overline{u} + u') \\
&E_q = \alpha_q T
\end{aligned} \tag{7}$$

In the above Eq. 5-7, Y is meridional direction in the ocean, U, V, are zonal and meridional currents, H is thermocline depth, τ_x is zonal wind stress and T is SST. Only a few processes deemed most important are retained in the SST budget from Eq. 6, such as dissipation by latent heat losses and the so-called thermocline feedback (An and Jin, 2001; Thual et al., 2016). Note that the ocean covers the equatorial Pacific domain only with boundary conditions at the western and eastern edges (see hereafter). The above system includes a minimal number of parameters: ϵ (Froude number), c_1, ζ, η, γ and α_q (see details in the appendix section B).

A few important remarks can be made on the coupling between the above ocean and SST model from Eq. 5-7 and the intraseasonal and interannual atmospheres from Eq. 2-3. Fig. 1(a) shows a sketch of the couplings in the complete TSS-GCM model derived hereafter. First, the ocean, SST and interannual atmosphere (Eq. 5-7 and Eq. 3) are coupled through latent heat release $E_q = \alpha_q T$ that forces an atmosphere circulation. The resulting zonal wind stress τ_x in return forces an ocean circulation that modifies the sea surface temperatures through thermocline depth anomalies H. In the absence of the intraseasonal atmosphere such a coupled interannual ocean-atmosphere system is linear, deterministic and stable and simulates a dissipated ENSO cycle with realistic period $\approx 4.5\,yr$ and overall structure (see SI of Thual et al., 2016). Second, the intraseasonal atmosphere (Eq. 2) is the starting skeleton model from Majda and Stechmann (2009) and intends to model the main features of the MJO. Here, such an intraseasonal atmosphere is fully coupled to the interannual atmosphere-ocean system. The intraseasonal wind bursts u' force the ocean through the wind stress τ_x in Eq. 7, and the ocean conditions modulate the intraseasonal atmosphere through interannual convective activity $\overline{a}$ in Eq. 2. Noteworthy, the intraseasonal atmosphere plays the role of triggering the ENSO in the otherwise dissipated ocean-atmosphere system, which is fundamentally different from the Cane-Zebiak (Zebiak and Cane, 1987) and other nonlinear models that rely instead on internal ocean instability. Finally, as shown in Fig. 1(a) in the complete TSS-GCM model convective noise is added to the intraseasonal atmosphere that depends on the interannual convective activity $\overline{a}$ (i.e. is multiplicative): the details of this convective stochastic parameterization will be introduced hereafter.

2.3 Crude Interannual Atmosphere

In the next subsections, in order to derive the complete TSS-GCM model we will first consider a hierarchy of cruder model versions. Those crude model versions have simplified dynamics and/or stochastics that allows us to understand the underlying processes in the more realistic complete TSS-GCM model. We introduce here first a crude interannual model, followed by a crude intraseasonal model before presenting the complete TSS-GCM model.

Fig. 1(b) shows a sketch of the couplings in the crude interannual model. In the crude interannual model, the intraseasonal dynamics are omitted in favor of a simple stochastic parameterization of intraseasonal wind bursts. This follows the prototype of many simple or intermediate depicting the relationship between the ENSO and wind bursts, where intraseasonal dynamics are not solved explicitly (e.g. Moore and Kleeman, 1999; Eisenman et al., 2005; Jin et al., 2007; Chen et al., 2015; Thual et al., 2016). Such a crude interannual model reads:

Crude Interannual Atmosphere

$$\begin{aligned}
&-y\overline{v} - \partial_x\overline{\theta} = 0\\
&y\overline{u} - \partial_y\overline{\theta} = 0\\
&-(\partial_x\overline{u} + \partial_y\overline{v}) = \overline{H}\overline{a} - s^\theta\\
&-\overline{Q}(\partial_x\overline{u} + \partial_y\overline{v}) = \overline{H}\overline{a} + s^q + E_q
\end{aligned} \tag{8}$$

along with

$$\begin{aligned}
&\partial_t\overline{a} = -\lambda(\overline{a} - \hat{a}) + \sqrt{\lambda\hat{a}\overline{a}}\dot{W}\\
&\overline{H}\hat{a} = (E_q + s^q - \overline{Q}s^\theta)/(1 - \overline{Q})
\end{aligned} \tag{9}$$

and with no intraseasonal fluctuations, i.e. $u', v', \theta', q', a' = 0$. Meanwhile, the ocean and SST are identical to the ones in the previous sections (Eq. 5-7). Here, a simple stochastic differential equation (SDE) for intraseasonal variability is considered (Chen and Majda, 2016a): in Eq. 9 the background convective activity $\overline{a}$ is perturbed by a white noise source $\dot{W}$ and relaxes to the deterministic value $\hat{a}$ at a rate $\lambda = (30\,day)^{-1}$. Importantly, the SDE involves a multiplicative noise which ensures that $\overline{a} \geq 0$ (as long as $\hat{a} \geq 0$) in the model consistent with the definition of convective activity in previous sections. In particular, the equilibrium probability distribution of

$\overline{a}$ relaxes to a Gamma distribution:

$$P(\overline{a}) = \frac{1}{\mu^k G(k)} \overline{a}^{k-1} \exp(-\overline{a}/\mu). \tag{10}$$

for which $\overline{a} \geq 0$ as shown in Fig. 2(d), with here parameters $k = 2$ and $\mu = \hat{a}/2$.

2.4 Crude Intraseasonal Atmosphere

We now formulate the crude intraseasonal model. Fig. 1(c) shows a sketch of the couplings in such a model. As compared to the crude interannual model presented above, such a model captures the dynamical details of intraseasonal variability. Such details are however simplified to some extent because some fundamental convective nonlinearites and associated noise features are missing, that will be introduced hereafter in the complete TSS-GCM model. Starting from the deterministic intraseasonal atmosphere from Eq. 2, simple perturbations (additive white noise sources) and dissipations are added. This reads:

Crude Intraseasonal Atmosphere

$$\begin{aligned}
&(\partial_t + d_u)u' - yv' - \partial_x\theta' = 0 \\
&yu' - \partial_y\theta' = 0 \\
&(\partial_t + d_u)\theta' - (\partial_x u' + \partial_y v') = \overline{H}a' \\
&(\partial_t + d_q)q' + \overline{Q}(\partial_x u' + \partial_y v') = -\overline{H}a' + \sigma_q \dot{W}_q \\
&(\partial_t + d_a)a' = \Gamma q'\overline{a}.
\end{aligned} \tag{11}$$

Meanwhile, the interannual atmosphere, ocean and SST are identical to the ones in previous sections (Eq. 3 and Eq. 5-7). As compared to the starting deterministic intraseasonal atmosphere from Eq. 2, moisture is perturbed in Eq. 11 by a white noise source $\dot{W}_q$ and uniform dissipations d_u, d_q, d_a are added consistent with the noise-dissipation energy balance (Hottovy and Stechmann, 2015; Stechmann and Hottovy, 2017). Here $d_u, d_q, d_a = (30\,day)^{-1}$, which is a natural dissipation time scale for intraseasonal variability. In addition, for simplicity the evolution of convective activity is linearized around the interannual mean value $\overline{a}$ (and remains approximately linear for

$\overline{a}$ varying on the slower interannual timescale). As a result, an important caveat of the present crude intraseasonal model is that total convective activity $\overline{a} + a'$ is not always positive (though $\overline{a}$ remains positive), which is a deficiency compared with the starting deterministic skeleton model formulation from Eq. 1 (Majda and Stechmann, 2009; 2011).

2.5 Complete Tropical Stochastic Skeleton GCM

We formulate the complete TSS-GCM model. Fig. 1(a) shows a sketch of the couplings in such a model. The TSS-GCM model includes all the features from the starting deterministic ocean and atmosphere, with in addition important design elements already introduced above with the crude interannual and crude intraseasonal models (Fig. 1b and c). As compared to those crude models the complete TSS-GCM model retains some fundamental nonlinearities and multiplicative noise features associated with convection in nature, which are common to conventional GCM models. As shown hereafter, such a convective parameterization allows the complete TSS-GCM model to capture more realistically some important features of wind bursts in nature. This includes intermittent wind bursts of varying strength and intensity, both easterly or westerly, with short lifespan around 10-30 days, sharp structure in both space and time and large zonal fetch. The complete TSS-GCM model reads:

Complete TSS-GCM Intraseasonal Atmosphere

$$\begin{aligned}
&(\partial_t + d_u)u' - yv' - \partial_x\theta' = 0 \\
&yu' - \partial_y\theta' = 0 \\
&(\partial_t + d_u)\theta' - (\partial_x u' + \partial_y v') = \overline{H}a' \\
&(\partial_t + d_q)q' + \overline{Q}(\partial_x u' + \partial_y v') = -\overline{H}a' + \sigma_q \dot{W}_q \\
&\partial_t a' = \Gamma q'(\overline{a} + a') - \lambda a' + \sqrt{\lambda(\overline{a} + a')\overline{a}}\dot{W}_a.
\end{aligned} \tag{12}$$

Meanwhile, the interannual atmosphere, ocean and SST are identical to the ones in previous sections (Eq. 3 and Eq. 5-7). The interannual convective activity $\overline{a}$ driven by the ocean (Eq. 3, 5-7) modulates the intraseasonal variability in Eq. 12: for instance, an increased $\overline{a}$ increases the growth/decay rate of a' which increases the overall amplitude of intraseasonal variability, and conversely for a decreased $\overline{a}$. In Eq. 12 we have added white noise sources terms $\dot{W}_q$, $\dot{W}_a$ and associated dissipations as in the crude intraseasonal atmosphere from Eq. 11, in addition to a suitable SDE for convective activity a' as in the crude intraseasonal atmosphere from Eq. 9. Such a SDE involves multiplicative noise ensuring that $a' + \overline{a} > 0$ in agreement with the starting deterministic skeleton model formulation from Eq. 1 (Majda and Stechmann, 2009; 2011). In fact, the time tendency $\partial_t a'$ in Eq. 12 is driven by $\Gamma q'(\overline{a} + a')$ as well as $-\lambda a' + \sqrt{\lambda(\overline{a} + a')\overline{a}}\dot{W}_a$, which both ensure that $a' + \overline{a} > 0$ when considered independently (Majda and Stechmann, 2009; 2011; Chen and Majda, 2016a), therefore $a' + \overline{a} > 0$ is ensured by splitting method. In particular, for $q' = 0$ the $a' + \overline{a}$ relaxes to a Gamma distribution as in Fig. 2(d).

2.6 Complete Tropical Stochastic Skeleton GCM with Dynamic Walker Circulation

Here a dynamic Walker circulation is introduced in the TSS-GCM model. Such a dynamic Walker circulation can be obtained for unbalanced external sources of cooling/moistening $s^\theta \neq s^q$ in any versions of the TSS-GCM model presented above (crude interannual, crude intraseasonal or complete TSS-GCM). Recall that wind divergence in Eq. 3 can alternatively be expressed as:

$$-(\partial_x \overline{u} + \partial_y \overline{v}) = (E_q + s^q - s^\theta)/(1 - \overline{Q}) \qquad (13)$$

In Eq. 13, $E_q + s^q - s^\theta \neq 0$ forces a background interannual atmosphere circulation, which can arise either from latent heat release fluctuations $E_q \neq 0$ driven by the ocean (5-7) as well as unbalanced external sources of cooling/moistening $s^\theta \neq s^q$. Such unbalanced external sources allow us to capture in a simple fashion the dynamic Walker circulation in the equatorial Pacific marked by mean westward trade winds and an overturning circulation in the upper troposphere (Chen and Majda, 2016b; Ogrosky and Stechmann, 2015) as well as an equilibrium zonal gradient of SST and thermocline depth in the ocean.

In the TSS-GCM model as well as the crude interannual and intraseasonal models introduced above, the external sources of cooling/moistening $s^\theta$and s^q are constant and representative of a simple background warm pool of cooling/moistening. This is shown in Fig. 2(a): for simplicity the external sources are balanced, i.e. $s^q = s^\theta$ are maximal at the western edge of the equatorial Pacific ($x = 0$) and minimal around the eastern edge ($x \approx 18\,000\,km$), as in nature (see e.g. Majda and Stechmann, 2011; Thual et al., 2014 for a similar parameterization). This accounts qualitatively for the increased convective activity over the Indian ocean/western Pacific and decreased convective activity in the eastern Pacific, although the profiles are unrealistic over the Atlantic Ocean. Note that although s^θ and s^q are here constant with time, their variations with seasons could be accounted for in a more complex setup. In the TSS-GCM model with dynamic Walker circulation, the external sources are instead unbalanced as in nature (Ogrosky and Stechmann, 2015), i.e. $s^q \neq s^\theta$ as shown in Fig. 2(b). For this we have slightly shifted the profile of s^θ. Despite the apparent similarity between s^q and s^θ in Fig. 2(b), note that the quantity $s^m = (s^q - \overline{Q}s^\theta)/(1-\overline{Q})$ that appears in the expression of $\overline{H}\overline{a}$ in Eq. 3 shows large zonal variations (yet remains positive to ensure $\overline{a} \geq 0$). As shown hereafter, such an unbalance introduces a fundamental ocean-atmosphere background circulation representative of the dynamic Walker circulation in nature on interannual timescale.

2.7 Intercomparison of model versions

Here we provide a summary and intercomparison of all model versions of the TSS-GCM model. The main features of all model versions are listed in Table 1, and are also contrasted with the ones of conventional GCMs. Those features will be detailed hereafter in the next sections.

The features summarized in Table 1 are as follows: first, conventional GCMs that retain the full complexity of the ocean-atmosphere system typically show common and systematic biases in representing the ENSO, MJO and background circulation altogether (Lin et al., 2006; Kim et al., 2009; Wittenberg et al., 2004; 2006; 2014; Guilyardi et al., 2016). This may include biases for the background mean state, ENSO intermittency and diversity as well as its non-Gaussian statistics, in addition to biases for the MJO amplitude, duration and propagation (with often a weak or even absent MJO).

Secondly, the complete TSS-GCM model (Sec. 3.3, Fig. 1a) in comparison shows great skill at capturing qualitatively the above processes, and is computationally much less costly. Recovered features include an irregular and intermittent ENSO cycle with El Niño events of varying strength and intensity, in addition to intermittent MJO events and wind bursts that are realistically confined to the western Pacific/Indian ocean region of convection yet realistically expand to the central Pacific during the onset of El Niño events. Note that the model reproduces Gaussian SST statistics which is also a common deficiency of GCM models, though it is able to capture occasional extreme El Niño events. As compared to previous work (Majda and Stechmann, 2009; 2011; Thual et al., 2016), only a few additional parameters (dissipation and noise intensity) need to be specified. The careful choice of SDE with multiplicative noise ensures that convective activity $a' + \overline{a}$ remains positive (Chen and Majda, 2016a).

Thirdly, the TSS-GCM model with Walker circulation (Sec. 3.4) is obtained from the complete TSS-GCM model simply by imposing unbalanced external sources of cooling/moistening, i.e. $s^\theta \neq s^q$. This allows us to capture a simple dynamic Walker circulation that consists of a cold tongue/warm pool region with associated cooling/heating in the ocean and convection/subsidence in the atmosphere. Note that such a dynamic Walker circulation can also be obtained in the crude interannual or crude intraseasonal models by imposing $s^\theta \neq s^q$.

Next, in the crude intraseasonal model (Sec. 3.2, Fig. 1b) the atmosphere is simplified in terms of noise source and main nonlinearities. Such a crude model captures both the ENSO and MJO in simple fashion, but misses important convective details. In particular, the simulated intraseasonal variability is dominated by excessive power from moist westward propagating Rossby waves and a weaker MJO in comparison. Finally, in the crude interannual model (Sec. 3.1, Fig. 1c) there are no intraseasonal atmospheric fluctuations but instead simple stochastic perturbations of the background convective activity $\overline{a}$, which is a prototype for most simple models with stochastic wind bursts (Moore and Kleeman, 1999; Eisenman et al., 2005; Jin et al., 2007; Chen et al., 2015; Thual et al., 2016). This allows the model to generate ENSO variability in simple fashion, although there is no dynamical intraseasonal variability.

In the next section, we analyze in details the main features of the TSS-GCM model as well as its versions as summarized in Table 1. The appendix section B provides additional technical details on the model formulation and numerical solving algorithm.

3 El Niño, the MJO and the dynamic Walker Circulation in the TSS-GCM model

In this section we show results from numerical experiments with the TSS-GCM model presented in previous section. Despite the model simplicity, the main features of interannual and intraseasonal variability are captured qualitatively. For clarity and consistency with the previous section, we introduce here the main features of each model version in order of increasing complexity: crude interannual, crude intraseasonal, complete TSS-GCM model and complete TSS-GCM model with dynamic Walker circulation.

3.1 Crude Interannual Model

We show here solutions of the crude interannual model (see Fig. 1b and Eq. 5-9 for its formulation). In the crude interannual model, the intraseasonal dynamics are omitted in favor of a simple stochastic parameterization of intraseasonal wind bursts with multiplicative features. This follows the prototype of many simple or intermediate models that describe the relationship between the ENSO and wind bursts, in which intraseasonal dynamics are not solved explicitly (e.g. Moore and Kleeman, 1999; Eisenman et al., 2005; Jin et al., 2007; Thual et al., 2016).

Fig. 3 show solutions of the crude interannual model. This includes the timeserie of T_E the average of SST anomalies in the eastern half of the equatorial Pacific (Fig. 3a), as well as the timeserie of convective activity $\overline{H}\overline{a}$ at the western edge of the Pacific (Fig. 3b). The T_E is a good indicator of El Niño variability in the model due to its possible comparison to e.g. the observed Niño3.SST index. The model simulates an ENSO cycle that is sustained, irregular and intermittent, as in nature (Clarke, 2008). While the evolution of T_E is essentially interannual, the evolution of $\overline{H}\overline{a}$ is both intraseasonal and interannual (cf 1-yr moving average, red) consistent with the SDE parameterization in Eq. 9. This illustrates the simple mechanisms for the generation of interannual variability in the model that results from the integration of noise: the interannual ocean-atmosphere system is here linear and dissipated while the SDE for $\overline{H}\overline{a}$ acts as an external source of perturbations. In addition to this, note that the probability density function (pdf) of T_E is nearly Gaussian while the pdf of $\overline{H}\overline{a}$ matches the theoretical Gamma distribution from Fig. 2(d) (not shown).

Fig. 3(c-g) shows the details of an El Niño event (around year 1623) with strong SST anomalies representative of extreme events in the observational record (e.g. 1997/98, 2015/16). The event starts with a realistic build-up of SST and thermocline depth anomalies in the western Pacific that eventually propagate and intensify in the eastern Pacific. Zonal winds anomalies become positive in the western to central Pacific consistent with the gradual weakening of the trade winds. The El Niño event is then followed by a reversal of conditions the following year towards a weak La Niña state.

3.2 Crude Intraseasonal Model

We now show solutions of the crude intraseasonal model (see Fig. 1c, Eq. 11 and Eq. 3, 5-7 for its formulation). As compared to the crude interannual model analyzed above, in the crude intraseasonal model the intraseasonal atmosphere dynamics are modelled. Important nonlinear and multiplicative noise features of convection are however not included that will be accounted for hereafter with the complete TSS-GCM model (Majda and Stechmann, 2009; Thual et al., 2014; Chen and Majda, 2016a). Another caveat of the crude intraseasonal model is the presence of unrealistic excessive westward propagation in the atmosphere.

An important feature as compared to the crude interannual model from previous section is that intraseasonal fluctuations are here dynamically resolved. Fig. 4(a,b,d,e) shows the power spectra of the intraseasonal atmosphere variables, as a function of the zonal wavenumber k (in $2\pi/40,000$ km) and frequency ω (in cpd). The intraseasonal atmosphere reproduces a MJO-like signal that is the dominant intraseasonal signal, consistent with observations (Wheeler and Kiladis, 1999; Thual et al., 2014; Stechmann and Hottovy, 2017). The MJO appears here as a sharp power peak in the intraseasonal-planetary band ($1 \leq k \leq 5$ and $1/90 \leq \omega \leq 1/30$ cpd), most prominent in u', q' and $\overline{H}a'$. This power peak roughly corresponds to the slow eastward phase speed of $\omega/k \approx 5\,ms^{-1}$

with the peculiar relation dispersion $d\omega/dk \approx 0$ found in observations. There is however excessive westward power in the intraseasonal band ($-3 \leq k \leq -1$ and $1/90 \leq \omega \leq 1/30$ cpd) as seen for θ', q' and a', which is a caveat of the present crude intraseasonal model. Note that power is maximal near the dispersion curves of the linear solutions of the intraseasonal atmosphere (black dots, see Thual et al., 2014 for a discussion).

In order to understand the timescale interaction between El Niño and the wind bursts, Fig. 4(c,f) shows the power spectrum of T_E the average of SSTs in the eastern Pacific, as well as u'_W the average of intraseasonal winds in the western Pacific half. The indice T_E is here a good indicator of the ENSO variability in the model while the indice u'_W is a good indicator of the wind bursts variability. Both power spectrum are shown in log-log scale to cover both the interannual and intraseasonal range, and the dashed lines indicate the intraseasonal 30-90 days band from Fig. 4(a,b,d,e). First, the spectrum of u'_w is approximately white (with power evenly distributed) except for fluctuations below 30 days that are dissipated. Associated with this, the spectrum of T_E is approximately red (i.e. decreasing linearly with frequency) consistent with the time-integration of noise by the interannual ocean and atmosphere. Second, the spectrum of T_E shows a peak at around $0.2\,yr^{-1}$ ($\approx 4.5\,yr$) that is consistent with the average period of the ENSO in nature and the linear solutions of the interannual atmosphere and ocean (Thual et al., 2016). Note in particular that details of intraseasonal variability in the 30-90 days are clearly separated from the average ENSO period.

Fig. 5 shows the details of intraseasonal variability during a strong El Niño event (around year 922). Consistent with the model formulation, the intraseasonal atmosphere evolves on a different timescales than the interannual atmosphere and ocean, with the exception of some intraseasonal disturbances on thermocline depth that correspond mainly to eastward propagating ocean Kelvin waves. Fig. 5(a) shows a data projection e_{MJO} that evaluates the MJO intensity by comparison to the linear solutions of the crude intraseasonal atmosphere. Such a data projection is obtained by filtering the intraseasonal atmosphere signals in the intraseasonal-planetary band ($1 \leq k \leq 3$, $1/90 \leq \omega \leq 1/30$ cpd), then projecting them on the MJO linear solution eigenvector (see Majda and Stechmann, 2011; Thual et al., 2014; Stechmann and Majda, 2015 for details). This representation, along with the other Hovmollers diagrams shown in Fig. 5, allows us to identify clearly the MJO variability despite the noisy signals. On average, the simulated MJO events propagate eastward with a phase speed $\approx 5 - 15\, ms^{-1}$ and period ≈ 40 days and are furthermore organized into wavetrains (i.e. series) of successive events, as in nature.

The El Niño event onset in Fig. 5 (around year 920 to 922) consists of a build-up of SST and thermocline depth anomalies starting from the western Pacific. During the event onset, intraseasonal wind bursts u', convective activity $\overline{H}a'$ and the MJO gradually intensify and expand towards the central to eastern Pacific, as in nature (Eisenman et al., 2005; Hendon et al., 2007; Tziperman and Yu., 2007; Gebbie et al., 2007). Some MJO wavetrains even reach the eastern Pacific during the event peak (around year 922). Note that in the absence of El Niño events, intraseasonal variability remains confined overall to the Indian ocean and western Pacific consistent with the increased sources of cooling/moistening s^{θ}, s^{q} over that region (cf Fig. 2a, Majda and Stechmann, 2011). Finally, strong wind bursts or a prominent MJO do not necessarily trigger El Niño events (Fedorov et al., 2015; Hu et al., 2014), as shown for example with the strong wind bursts in Fig. 5 around year 919.5. Note in addition the presence of excessive westward propagations in Fig. 5 on wind bursts u', potential temperature θ' and moisture q', which is a caveat of the present crude intraseasonal model.

3.3 Complete Tropical Stochastic Skeleton GCM Model

We now show the solutions of the complete TSS-GCM model (see Fig. 1a, Eq. 12 and Eq. 3, 5-7 for its formulation). Such a model retains all the dynamics from the starting deterministic ocean and atmosphere, elements from the crude interannual and intraseasonal model versions presented above, in addition to fundamental convective nonlinearities and associated suitable stochastic parameterizations. This allows the complete TSS-GCM model to capture realistically some important features of wind bursts in nature. Such features include intermittent wind bursts of varying strength and intensity, both easterly or westerly, with short lifespan around 10-30 days, sharp structure in both space and time and large zonal fetch. Associated with those wind bursts are sharp and localized peaks of convective activity as representative of deep convective events in nature.

For completeness, several diagnostics presented above for the crude interannual and intraseasonal model versions are repeated here for the complete TSS-GCM model.

Fig. 6 shows the details of a super El Niño event (around year 1096.8) simulated by the complete TSS-GCM model. Importantly, there are here more realistic intraseasonal and convective features as compared to the crude intraseasonal model (Fig. 5). This includes localized wind bursts (u' in Fig. 6c) in the western Pacific, both easterly or westerly, with short lifespan around 10-30 days, sharp structure in both space and time and large zonal fetch. Those wind bursts result from strong and localized peaks in convective activity ($\overline{H}(\overline{a} + a')$ in Fig. 6d) as representative of deep convective events in nature, with heating reaching $1\,K.day^{-1}$ or more while convection is otherwise suppressed overall ($\approx 0.1\,K.day^{-1}$). Such a realistic bursting behavior in both convection and wind bursts result from the parameterization of convection in Eq. 12 with non-Gaussian noise and fundamental nonlinearities. In addition to this, the complete TSS-GCM model captures the eastward expansion of the sharp wind bursts and convective events during the onset of the El Niño event (Eisenman et al., 2005; Hendon et al., 2007; Tziperman and Yu., 2007; Gebbie et al., 2007). This is best seen in Fig. 6(c) on total zonal winds $\overline{u}+u'$, for which westerly wind bursts are dominant in the western Pacific/Indian ocean at the event onset (1095.8 to 1096 yr) then gradually expand towards the eastern Pacific until the event peak (around 1096.8). Those are all important and realistic features captured in a simple fashion by the complete TSS-GCM model. Note that the total convective activity $\overline{a} + a'$ remains positive in Fig. 6(d) which is in agreement with the design principles for the model's atmosphere (Eq. 1, 12).

Fig. 7 shows timeseries and hovmollers for the interannual variability simulated by the complete TSS-GCM model. The model simulates a sustained and irregular ENSO cycle with intermittent El Niño and La Niña events of varying intensity and strength, as in nature (Clarke, 2008). In Fig. 7, there are in particular two super El Niño events with strong SST anomalies representative of extreme events in the observational record (e.g. 1997/98, 2015/16), realistically separated by around 20 years. Those super El Niño events start with a build-up of SST and thermocline depth anomalies in the western Pacific that eventually propagate and intensify in the eastern Pacific, in addition to a gradual increase in zonal winds anomalies, as in nature. There are in addition many examples of moderates or failed El Niño events in Fig. 7. There are however no central Pacific events simulated by the model, though this could be improved with the addition of nonlinear advection of SST in the model's SST budget (Chen and Majda, 2016b; 2017; Chen et al., 2018). Fig. 7(c) shows a one-year running mean of $|e_{MJO}|$ the magnitude of the data projection e_{MJO}. This allows us to evaluate the interannual variations of the MJO intensity. The interannual variations of the MJO intensity are random overall as resulting from the internal variability of the intraseasonal atmosphere alone (see e.g. Fig. 5 of Thual et al., 2014 for comparison), though they are here modulated to some extent by the SSTs. For instance, the MJO intensity in Fig. 7(c) is increased from the western to eastern Pacific during some El Niño events.

The present TSS-GCM model provides the upscale contribution of intraseasonal wind bursts and the MJO to the interannual flow as well as their modulation in return in an explicit way. For this, Fig. 8 shows lagged regressions of several interannual and intraseasonal variables on T_E the average of SST in the Pacific eastern half. This highlights the overall formation mechanisms and chronology of El Niño events in the model. In order to identify the evolution of the intraseasonal atmosphere evolution during El Niño, we consider lagged regressions for the data projection e_{MJO} (cf Fig. 6) and intraseasonal zonal winds u' as well as their magnitude.

As shown in Fig. 8, El Niño events typically start with increased thermocline depth and SST anomalies in the western Pacific that eventually propagate to the eastern Pacific, in addition to gradually increasing interannual winds. Those features are overall consistent with the hovmollers in Fig. 7. Interestingly, the magnitude of intraseasonal variability in general ($|e_{MJO}|$ and $|u'|$ in Fig. 8b,d) is increased overall in the western Pacific during the onset of El Niño as well as in the central to eastern Pacific during the event peak, as in nature (Vecchi and Harrison, 2000; Hendon et al., 1999). In the TSS-GCM model, the gradual increase and expansion of intraseasonal variability from the western to eastern Pacific results from the increased SSTs that favor the temporal growth/decay of convective activity a' (cf Eq. 12). Next, results suggest that the upscale contributions of the wind bursts play a key role for the triggering of El Niño events, but not the upscale contribution of the MJO. First, wind bursts u' in Fig. 8(c) are predominantly westerly in the western to central Pacific around 6 months prior to the event peak (e.g. Hu and Fedorov, 2017). In fact, westerly wind bursts force a deepening of the equatorial thermocline in the ocean (i.e. downwelling equatorial ocean Kelvin and Rossby waves) that further contribute to the increase of El Niño SSTs. Interestingly, the location and timing of those predominantly westerly wind bursts in Fig. 8(c) does not match the one of the overall increased magnitude ($|u'|$ in Fig. 8d), suggesting that only some wind bursts may be key for the triggering of the El Niño events. Recall in addition that wind bursts from the intraseasonal atmosphere trigger the El Niño by design in the TSS-GCM model because they are coupled to an interannual atmosphere that is otherwise stable, linear and dissipated (cf Eq. 3, 5-7; see also Thual et al., 2016 for a discussion). On the other hand, lagged regressions with El Niño SSTs are weak for MJO variability (e_{MJO} in Fig. 8a), except during the event peak for which they match overall the increased (decreased) convection in the eastern (western) Pacific. In fact, the MJO approximately oscillates at a period ≈ 40 days with opposite and canceling effects on the ocean that are ineffective at triggering El Niño events despite an increased magnitude $|e_{MJO}|$.

Finally, other features of the intraseasonal atmosphere such as its power spectra and statistics are overall consistent with nature. First, Fig. 9(a,b,e,f) shows the power spectra for variables of the intraseasonal atmosphere in the complete TSS-GCM model. While the features are overall similar to the ones of the crude intraseasonal model version (Fig. 4), there are here less westward propagations in the intraseasonal 30-90 days band as seen for u' as well as q' and θ', which is more realistic. Second, in order to understand the timescale interaction between El Niño and the wind bursts, Fig. 9(c,g) shows the power spectrum of T_E the average of SSTs in the eastern Pacific, as well as the power spectrum of u'_W the average of intraseasonal wind bursts in the western Pacific half. As compared to the crude interannual atmosphere model version (Fig. 4), the spectrum of u'_w is here not entirely white: for instance, it shows a slight peak around $0.2\,yr^{-1}$ ($\approx 4.5\,yr$) similar to the one on the power spectrum of T_E, which corresponds to the average ENSO period in the model. This shows that wind bursts variability is modulated interannualy to some extent by ENSO SSTs, consistent with the lagged regressions in Fig. 8 (d). Finally, Fig. 9(d,h) shows the probability density functions (pdfs) for T_E as well as total convective activity $\overline{H}(a' + \overline{a})$ at the Pacific western edge. The pdf of T_E is nearly Gaussian, in slight discrepancy with the skewed distribution of eastern Pacific SSTs in observations (e.g. Niño 3 SST). Such a discrepancy is also common in GCMs, and could likely be improved by rendering the stochastic noise in the intraseasonal atmosphere more multiplicative (Jin et al., 2007; Thual et al., 2016). Meanwhile the pdf of $\overline{H}(a'+\overline{a})$ matches to some extent the theoretical Gamma distribution from Eq. 10 and Fig. 2(d) (which ensures notably that $a'+\overline{a}$ remains positive, Chen and Majda, 2016a), though it is significantly more skewed towards extreme convective events due to the addition of deterministic convective nonlinearities in the complete TSS-GCM model ($\Gamma q'(\overline{a}+a')$ in Eq. 12).

3.4 Complete TSS-GCM model with Dynamic Walker Circulation

We now show solutions of the TSS-GCM model with Dynamic Walker Circulation. Such a model version is identical to the TSS-GCM model presented above except for the introduction of unbalanced external sources of cooling/moistening $s^\theta \neq s^q$ (Fig. 2b). This allows to capture in simple fashion the dynamic Walker circulation in the equatorial Pacific marked by mean westward trade winds and an overturning circulation in the upper troposphere, (Chen and Majda, 2016b; Ogrosky and Stechmann, 2015) as well as an equilibrium zonal gradient of SST and thermocline depth in the ocean. Note that a dynamic Walker circulation can be obtained for $s^\theta \neq s^q$ in any versions of the TSS-GCM model (crude interannual, crude intraseasonal or complete TSS-GCM).

Fig. 10 shows the background mean (i.e. climatological) circulation, obtained from a time-average of the model solutions. The equilibrium atmosphere consists of a region of ascent, convergence and increased convection in the western Pacific as well as subsidence and divergence in the eastern Pacific. Those are all realistic features representative of the Walker circulation in nature. Note that the present atmosphere has a first baroclinic mode structure, with reconstruction $\overline{u}=\overline{u}(x)cos(z)$ as well as $\overline{w}=-\partial_x\overline{u}\sin(z)$ (see e.g. Chen and Majda, 2016b). Meanwhile, the equilibrium atmospheric circulation maintains realistic zonal gradients of SST ($\approx 8K$) and thermocline depth ($\approx 200m$) in the ocean, which intensities compare reasonably with the ones found in nature (Clarke, 2008). Finally, the intraseasonal and interannual features of the present model version are similar to the ones of the complete TSS-GCM model (Fig. 9-7), and are not shown for brevity.

4 Discussion

In the present article, a simple dynamical stochastic model for the ENSO, MJO and intraseasonal variability in general as well as the dynamic Walker circulation has been introduced and developed in details. The present model, the so-called 'Tropical Stochastic Skeleton GCM' model (TSS-GCM model) serves as a prototype for General Circulation Models (GCMs) that solve similar dynamical interactions across several spatio-temporal scales but usually show common and systematic biases in representing tropical variability as a whole. The present model formulation builds on previous work by the authors, namely a simple deterministic ocean-atmosphere for the ENSO (Thual et al., 2014; 2016; 2017; Chen and Majda, 2016b; 2017; Chen et al., 2018) in addition to a skeleton model for the MJO and intraseasonal variability in general (Majda and Stechmann, 2009; 2011; Thual et al., 2014). In particular, a simple decomposition of the atmospheric flow in the present TSS-GCM model allows us to represent in simple fashion both the interannual and intraseasonal dynamics as well as their interactions. The most salient features of the ENSO, wind bursts and the MJO are captured altogether including their overall structure, evolution and energy distribution across scales, in addition to their intermittency and diversity as well as their fundamental interactions. The model developed here also should be useful to diagnose, analyze and help eliminate the strong tropical biases which exist in current operational models.

Generally speaking, GCMs typically show common and systematic biases in representing the ENSO, MJO and background circulation altogether (Lin et al., 2006; Kim et al., 2009). This is because they solve a vast range of strongly interacting processes on many spatial and temporal scales. The present TSS-GCM model in comparison shows great skill at capturing qualitatively both intraseasonal and interannual processes. This provides theoretical insight on the essential dynamics and interactions of such processes, which is a main goal of the present work. As compared to former studies dealing with the ENSO and wind burst activity (Moore and Kleeman, 1999; Eisenman et al., 2005; Tziperman and Yu., 2007; Lopez et al., 2013), the present model features wind bursts that are dynamically solved. For instance, there is no arbitrary prescription of wind bursts amplitudes, propagations or abrupt convection thresholds. In addition, for simplicity intraseasonal wind bursts are coupled to ocean-atmosphere processes that are otherwise deterministic, linear and dissipated. Wind bursts that trigger El Niño events in the model are preferentially westerly, with however many examples of mixed westerly and easterly wind bursts, a situation commonly encountered for example within the convective envelope of the MJO (Hendon et al., 2007; Majda and Stechmann, 2011; Puy et al., 2016). In addition to this, wind bursts in the model are a necessary but non-sufficient condition to El Niño development, as many wind bursts are not followed by El Niño events, as in nature (Fedorov et al., 2015; Hu et al., 2014). These are attractive features of the present dynamical stochastic model.

A more complete model should account for more details of the ocean-atmosphere dynamics relevant to ENSO. For example, the SST budget could include additional processes such as zonal advection that is deemed essential for the dynamics of central Pacific El Niño events (Ashok et al., 2007; Chen and Majda, 2016b; 2017 Chen et al., 2018). In addition to this, the models SST statistics may be rendered more non-Gaussian (i.e. skewed towards rare extreme El Niño events) by modifying the stochastic noise associated with intraseasonal convection to be more multiplicative (Jin et al., 2007; Thual et al., 2016). Meanwhile, a more detailed representation of the intraseasonal wind burst activity should be included in the model. For instance, while the skeleton model atmosphere used in the present appears to be a plausible representation of the MJO essential mechanisms (Majda and Stechmann, 2009; 2011; Thual et al., 2014), due to its minimal design it does not account for some processes that generate wind bursts including tropical cyclones or extratropical cold surges (Harrison and Vecchi, 1997; Vecchi and Harrison, 2000; Kiladis et al., 2009; Chen et al., 2016). A more complete model should also account for more detailed sub-planetary processes within the MJO's envelope, including for example synoptic-scale convectively coupled waves and/or mesoscale convective systems (Thual and Majda, 2015). This may achieved for example by building suitable stochastic parameterizations, such as the one proposed in the present article, that account for more details of the synoptic and/or mesoscale variability (e.g., Khouider et al., 2010; Frenkel et al., 2012; Deng et al., 2014).

Acknowledgments

The research of A. J. M. is partially supported by the Office of Naval Research grant ONR MURI N00014 -12-1-0912 and the center for Prototype Climate Modeling at the NYU Abu Dhabi

Research Institute. S.T. and N.C are supported as postdoctoral fellows through A.J.M's ONR MURI grant.

Appendix A: Derivation of the Starting Deterministic Atmosphere

This section details the derivation of the starting deterministic atmosphere used in the TSS-GCM model from a multiple time approach (Majda and Klein, 2003). A general motivation for this is to derive approximate solutions for slowly varying fluctuations in the atmosphere. For this, we assume the Reynolds hypothesis that such slowly varying fluctuations exists on the interannual time τ, in addition to fastly varying fluctuations on the intraseasonal time t with zero mean on the slow time. Assuming the Reynolds hypothesis, the starting atmosphere from Eq. 1 is decomposed as:

$$\begin{aligned} a(x,y,t) &= \overline{a}(x,y,\epsilon t) + a'(x,y,\epsilon t,t), \text{ i.e.} \\ a(x,y,\tau,t) &= \overline{a}(x,y,\tau) + a'(x,y,\tau,t) \end{aligned} \tag{14}$$

and similarly for u, v, θ, q, with the relation between time variables $\tau = \epsilon t$ where ϵ (the Froude number) is an asymptotically small parameter. SSTs however show weak intraseasonal variability in nature, therefore associated latent heat release decomposes as $E_q = \overline{E}_q + \epsilon E'_q$. The Reynolds operator is defined here as:

$$\overline{a}(x,y,\tau) = \frac{1}{\Delta\tau} \int_{\tau+\Delta\tau/2}^{\tau+\Delta\tau/2} a(x,y,\tau,t)dt \tag{15}$$

where $\Delta\tau$ is a characteristic averaging interannual timescale. Note that for $\Delta\tau = \Delta t/\epsilon$, $\epsilon \to 0$ with Δt constant the above Reynolds operator is asymptotically akin to a Reynolds time-mean average as in standard turbulence theory. Such an operator has the well-known properties $\partial_t \overline{a} = 0$, $\overline{a'} = 0$ as well as $\partial_t a = \epsilon\partial_\tau \overline{a} + (\epsilon\partial_\tau + \partial_t)a'$. Next, we further decompose the variables in Eq. 14 into powers of ϵ small, i.e. $a = a_0 + \epsilon a_1 + O(\epsilon^2)$. Combined with the above Reynolds decomposition, this reads:

$$a(x,y,\tau,t) = \overline{a}_0(x,y,\tau) + a'_0(x,y,\tau,t) + \epsilon\overline{a}_1(x,y,\tau,t) + \epsilon a'_1(x,y,\tau,t) + O(\epsilon^2) \tag{16}$$

The crucial requirements needed to formally guarantee that the terms $a_0 = \overline{a}_0 + a'_0$ describes the leading-order behavior in Eq. 16 are the sublinear growth conditions for the next order terms $a_1 = \overline{a}_1 + a'_1$:

$$\lim_{\epsilon\to 0}\left(\frac{a_1(x,y,\tau,\tau/\epsilon)}{|\tau/\epsilon|+1}\right) = 0. \tag{17}$$

In order to obtain the interannual atmosphere, we decompose the starting atmosphere from 1 according to Eq. 16 and retain the leading order dynamics (of order $O(1)$). This reads:

$$\begin{aligned}
&-y\overline{v}_0 - \partial_x\overline{\theta}_0 = 0\\
&y\overline{u}_0 - \partial_y\overline{\theta}_0 = 0\\
&-(\partial_x(\overline{u} + \partial_y\overline{v}_m) = \overline{H}\overline{a}_0 - s^\theta\\
&\overline{Q}(\partial_x\overline{u}_m + \partial_y\overline{v}_m) = -\overline{H}\overline{a}_0 + s^q + \overline{E}_{q0}\\
&0 = \overline{q_0}\;\overline{a_0} + \overline{q'_0 a'_0}
\end{aligned} \tag{18}$$

where a simple closure $\overline{q'_0 a'_0} \propto \overline{q_0}$ is considered for the upscale contribution, leading to $\overline{q_0} = 0$. With this simple closure, we retrieve the interannual atmosphere from Eq. 3 in the main text. Finally, the intraseasonal atmosphere from Eq. 2 is obtained by subtracting Eq. 3 from Eq. 1 , and the subscript notation a_0 is dropped for brevity.

Appendix B: Technical Details

We provide here some additional technical details on the TSS-GCM model formulation and numerical solving algorithm. As regards the atmosphere and ocean domains, the atmosphere extends over the entire equatorial belt $0 \le x \le L_A$ with periodic boundary conditions $u(0,y,t) = u(L_A,y,t)$, etc, while the Pacific ocean extends from $0 \le x \le L_O$ with reflection boundary conditions $\int_{-\infty}^{+\infty} U(0,y,t)dy = 0$ and $U(L_O,y,t) = 0$. The meridional axis y and Y are different in the atmosphere and ocean as they each scale to a suitable Rossby radius, which allows for a systematic meridional decomposition of the system into the well-known parabolic cylinder functions (Majda, 2003). In practice, we retain and solve only the components of the first atmosphere and ocean parabolic cylinder functions, which keeps the system low-dimensional (see Supplementary Information of Thual et al., 2016). The dimensional reference scales are x: 15000 km, y : 1500km, Y : 330km, t: 3.3 days, u: $5\,m.s^{-1}$, θ, q: 1.5 K (see Thual et al., 2016). Table 2 defines all parameter used in the model and provides their non-dimensional values. All parameter values are identical to the ones of Thual et al. (2016), except for additional parameters of the intraseasonal atmosphere: s^q and s^θ (see Fig. 2), $\Gamma = 1.66$ ($\approx 0.3\,K^{-1}day^{-1}$ as in Thual et al., 2014), $d_u, d_\theta, d_q, d_a, \lambda = (30\,day)^{-1}$ as well as $\sigma_q = 0.4$. In addition, the zonal profile of the thermocline feedback parameter $\eta(x)$ is shown in Fig. 2(c).

As regards the numerical solving algorithm, we use a simple split method to update the TSS-GCM model. The spatial resolution is 625 km and the temporal resolution is 0.8 hr. The interannual atmosphere and ocean are solved in fashion identical to Thual et al. (2016) using the method of lines in space and Euler in time, while the intraseasonal atmosphere is solved in Fourier space in fashion similar to Thual et al. (2014). Numerical solutions span around 2000 years for each experiment presented in the present article, with a statistical equilibrium quickly reached after around ten years starting from arbitrary initial conditions. It takes around 3 hours to compute 2000 years of simulation on a personal desktop, which is computationally very uncostly.

References

An, S.-I. and Jin, F.-F. (2001). Collective role of thermocline and zonal advective feedbacks in the ENSO mode. *J.Climate*, 14(16):3421–3432.

Ashok, K., Behera, S. K., Rao, S. A., Weng, H., and Yamagata, T. (2007). El Nino Modoki and its possible teleconnections. *J. Geophys. Res*, 112.

Chen, D., Lian, T., Fu, C., Cane, M., Tang, Y., Murtugudde, R., Song, X., Wu, Q., and Zhou, L. (2015). Strong influence of westerly wind bursts on El Nino diversity. *Nature Geoscience*, 8:339–345.

Chen, N. and Majda, A. (2016a). Filtering the Stochastic Skeleton Model for the Madden-Julian Oscillation. *Mon.Wea.Rev.*, 144:501–527.

Chen, N. and Majda, A. (2016b). Simple dynamical models capturing the key features of the central pacific El Nino. *Proc. Natl. Acad. Sci.*, 113:11732–11737.

Chen, N. and Majda, A. (2017). Simple Stochastic Dynamical Models Capturing the Statistical Diversity of El Nino Southern Oscillation. *Proc. Natl. Acad. Sci.*, 113(42):11732–11737.

Chen, N., Majda, A., and Thual, S. (2018). Observations and mechanisms of a simple stochastic dynamical model capturing El Nino diversity. *J.Clim.*, (31):449–471.

Chen, S., Majda, A., and Stechmann, S. (2016). Tropical-Extratropical Interactions with the MJO Skeleton and Climatological Mean Flow. *J.Atm.Sci.*, 73(10):4101–4116.

Christensen, H., Berner, J., Coleman, D., and Palmer, T. (2017). Stochastic Parameterization and El Nino-Southern Oscillation. *J.Clim.*, 17:17–38.

Clarke, A. J. (2008). *An Introduction to the Dynamics of El Nino & the Southern Oscillation*. Academic Press.

Deng, Q., Khouider, B., and Majda, A. J. (2014). The MJO in a Coarse-Resolution GCM with a Stochastic Multicloud Parameterization. *J. Atmos. Sci.*, 72. 55-74.

Eisenman, I., Yu, L., and Tziperman, E. (2005). Westerly Wind Bursts: ENSO's Tail Rather than the Dog? *J. Climate.*, 18:5224–5238.

Fedorov, A., Hu, S., Lengaigne, M., and Guilyardi, E. (2015). The impact of westerly wind bursts and ocean initial state on the development, and diversity of El Nino events. *Clim. Dyn.*, 44:1381–1401.

Frenkel, Y., Majda, A. J., and Khouider, B. (2012). Using the Stochastic Multicloud Model to Improve Tropical Convective Parameterization: A Paradigm Example. *J. Atmos. Sci.*, 69:1080–1105.

Gebbie, G., Eisenman, I., Wittenberg, A., and Tziperman, E. (2007). Modulation of Westerly Wind Bursts by Sea Surface Temperature: A Semistochastic Feedback for ENSO. *J. Atm. Sci.*, 64:3281–3295.

Gill, A. (1980). Some simple solutions for heat-induced tropical circulation. *Quart. J. Roy. Meteor. Soc.*, 106:447–462.

Goswami, B., Khouider, B., Phani, R., Mukhopadhyay, P., and Majda, A. (2017). Improved Tropical Modes of Variability in the NCEP Climate Forecast System (Version 2) via a Stochastic Multicloud Model. *J.Atm.Sci.*, 74(10):3339–3366.

Goswami, B. B., Khouider, B., Phani, R., Mukhopadhyay, P., and Majda, A. (2016). Improving synoptic and intraseasonal variability in CFSv2 via stochastic representation of organized convection. *Geophys. Res. Lett.*, 44(2):1104–1113.

Guilyardi, E., Wittenberg, A., Balmaseda, M., Cai, W., Collins, M., M.K., M., Watanabe, M., and Yeh, S.-W. (2016). Fourth CLIVAR Workshop on the Evaluation of ENSO Processes in Climate Models: ENSO in a Changing Climate. *Bulletin of the American Meteorological Society*, 97(5):817–820.

Gushchina, D. and Dewitte, B. (2011). The relationship between intraseasonal tropical variability and ENSO and its modulation at seasonal to decadal timescales. *Cent.Eur.J.Geosci.*, 1:175–196.

Harrison, D. and Vecchi, G. (1997). Westerly wind events in the tropical Pacific. *J. Climate*, 10:3131–3156.

Hendon, H., Wheeler, M., and Zhang, C. (2007). Seasonal Dependence of the MJO-ENSO Relationship. *J. Climate.*, 20:543.

Hendon, H. H., Zhang, C., and Glick, J. (1999). Interannual Variation of the Madden-Julian Oscillation during Austral Summer. *J. Climate*, 12:2538–2550.

Hottovy, S. and Stechmann, S. (2015). A Spatiotemporal Stochastic Model for Tropical Precipitation and Water Vapor Dynamics. *J.Atm.Sci.*, 72:4721–4738.

Hu, S. and Fedorov, A. (2017). The extreme El Nino of 2015-2016: the role of westerly and easterly wind bursts, and preconditioning by the failed 2014 event. *Clim. Dyn.*, 43. doi:10.1007/s00382-017-3531-2.

Hu, S., Fedorov, A., Lengaigne, M., and Guilyardi, E. (2014). The impact of westerly wind bursts on the diversity and predictability of El Nino events: An ocean energetics perspective. *Geophys. Res. Lett.*, 41:4654–4663.

Jin, F.-F., Lin, L., Timmermann, A., and Zhao, J. (2007). Ensemble-mean dynamics of the ENSO recharge oscillator under state-dependent stochastic forcing. *Geophys. Res. Lett.*, 34:doi:10.1029/2006GL027372.

Khouider, B., Biello, J. A., and Majda, A. J. (2010). A Stochastic Multicloud Model for Tropical Convection. *Comm. Math. Sci.*, 8(1):187–216.

Kiladis, G. N., Wheeler, C., Haertel, P. T., Straub, K. H., and Roundy, P. E. (2009). Convectively coupled equatorial waves. *Rev. Geophys.*, 47. RG2003, doi:10.1029/2008RG000266.

Kim, D., Sperber, K., Stern, W., Waliser, D., Kang, I.-S., Maloney, E., Wang, W., Weickmann, K., Benedict, J., Khairoutdinov, M., Lee, M.-I., Neale, R., Suarez, M., Thayer-Calder, K., and Zhang, G. (2009). Application of MJO simulation diagnostics to climate models. *J. Climate*, 22:6413–6436.

Kleeman, R. (2008). Stochastic theories for the irregularity of ENSO. *Phil. Trans. R. Soc*, 366:2509–2524.

Kleeman, R. and Moore, A. (1997). A theory for the limitation of ENSO predictability due to stochastic atmospheric transients. *J. Atmos Sci*, 54:753–767.

Lin, J.-L., Kiladis, G. N., Mapes, B. E., Weickmann, K. M., Sperber, K. R., Lin, W., Wheeler, M. C., Schubert, S. D., Del Genio, A., Donner, L. J., Emori, S., Gueremy, J.-F., Hourdin, F., Rasch, P. J., Roeckner, E., and Scinocca, J. F. (2006). Tropical Intraseasonal Variability in 14 IPCC AR4 Climate Models. Part I: Convective Signals. *J. Climate*, 19:2665–2690.

Lopez, H., Kirtman, B., Tziperman, E., and Gebbie, G. (2013). Impact of interactive westerly wind bursts on CCSM3. *Dyn. Atm. Oceans*, 59:24–51.

Madden, R. E. and Julian, P. R. (1971). Detection of a 40-50 day oscillation in the zonal wind in the tropical Pacific. *J. Atmos. Sci.*, 28:702–708.

Madden, R. E. and Julian, P. R. (1994). Observations of the 40-50 day tropical oscillation-A review. *Mon. Wea. Rev.*, 122:814–837.

Majda, A. and Klein, R. (2003). Systematic Multiscale Models for the Tropics. *J.Atm.Sci.*, 60:393–408.

Majda, A., Stechmann, S., Ogrosky, R., Chen, C., and Thual., S. (2018). *Explaining Tropical Intraseasonal Variability with the Stochastic Skeleton Model.* SpringerBriefs in Mathematics of Planet Earth: Weather, Climate, Oceans.

Majda, A. J. (2003). *Introduction to PDEs and Waves for the Atmosphere and Ocean. Courant Lecture Notes in Mathematics, Vol 9.* American Mathematical Society. Providence, x+234pp.

Majda, A. J., Franzke, C., and Khouider, B. (2008). An applied mathematics perspective on stochastic modelling for climate. *Philosophical Transactions of the Royal Society A: Mathematical, Physical and Engineering Sciences*, 366(1875):2427–2453.

Majda, A. J. and Stechmann, S. N. (2009). The skeleton of tropical intraseasonal oscillations. *Proc. Natl. Acad. Sci.*, 106:8417–8422.

Majda, A. J. and Stechmann, S. N. (2011). Nonlinear Dynamics and Regional Variations in the MJO Skeleton. *J. Atmos. Sci.*, 68:3053–3071.

McPhaden, M., Zhang, X., Hendon, H., and Wheeler, M. (2006). Large scale dynamics and MJO forcing of ENSO variability. *Geophys.Res.Lett.*, 33:1–5.

Moore, A. M. and Kleeman, R. (1999). Stochastic Forcing of ENSO by the Intraseasonal Oscillation. *J. Climate*, 12:1199–1220.

Neelin, J. D., Battisti, D. S., Hirst, A. C., Jin, F.-F., Wakata, Y., Yamagata, T., and Zebiak, S. E. (1998). ENSO theory. *Journal of Geophysical Research: Oceans*, 103(C7):14261–14290.

Neelin, J. D. and Zeng, N. (2000). A quasi-equilibrium tropical circulation model:formulation. *J. Atmos. Sci.*, 57:1741–1766.

Ogrosky, H. R. and Stechmann, S. N. (2015). The MJO skeleton model with observation-based background state and forcing. *Quart. J. Roy. Meteor. Soc.*, 141. 2654-2669.

Palmer, T. N. (2012). Towards the probabilistic Earth-system simulator: a vision for the future of climate and weather prediction. *Quart. J. Roy. Meteor. Soc.*, 138:841–861.

Puy, M., Vialard, J., Lengaigne, M., and Guilyardi, E. (2016). Modulation of equatorial Pacific westerly/easterly wind events by the Madden-Julian oscillation and convectively-coupled Rossby waves. *Clim. Dyn.*, 46:2155–2178.

Stachnik, J. P., Waliser, D. E., Majda, A., Stechmann, S., and Thual, S. (2015). Evaluating MJO initiation and decay in the skeleton model using an RMM-like index. *J. Geophys. Res. Atmos.*, 120(5):486–508.

Stechmann, S. and Hottovy, S. (2017). Unified spectrum of tropical rainfall and waves in a simple stochastic model. *Geophys.Res. Lett.*, 44(10):10713–10724.

Stechmann, S. N. and Majda, A. J. (2015). Identifying the skeleton of the Madden-Julian oscillation in observational data. *Mon. Wea. Rev.*, 143:395–416.

Thual, S., Majda, A., and Chen, N. (2017). Seasonal Synchronization of a Simple Stochastic Dynamical Model Capturing El Nino Diversity. *J.Climate*, 30(24):10047–10066.

Thual, S., Majda, A., Chen, N., and Stechmann, S. (2016). Simple Stochastic Model for El Nino with Westerly Wind Bursts. *Proc. Natl. Acad. Sci.*, 113(37):10245–10250.

Thual, S. and Majda, A. J. (2015). A skeleton model for the MJO with refined vertical structure. *Clim. Dyn.*, 46. doi:10.1007/s00382-015-2731-x.

Thual, S., Majda, A. J., and Stechmann, S. N. (2014). A stochastic skeleton model for the MJO. *J. Atmos. Sci.*, 71:697–715.

Tziperman, E. and Yu., L. (2007). Quantifying the Dependence of Westerly Wind Bursts on the Large-Scale Tropical Pacific SST. *J. Climate.*, 20:2760–2768.

Vecchi, G. and Harrison, D. (2000). Tropical Pacific sea surface temperature anomalies, El Nino, and equatorial westerly wind events. *J.Climate*, 13(11):1814–1830.

Weisheimer, A., Corti, S., Palmer, T., and Vitart, F. (2014). Addressing model error through atmospheric stochastic physical parametrizations: impact on the coupled ECMWF seasonal forecasting system. *Phil.Trans.Roy.Soc.A*, 372:20130290.

Wheeler, M. and Kiladis, G. N. (1999). Convectively Coupled Equatorial Waves: Analysis of Clouds and Temperature in the Wavenumber-Frequency Domain. *J. Atmos. Sci.*, 56:374–399.

Wittenberg, A., Rosati, A., Delworth, T., Vecchi, G., and Zeng, F. (2014). ENSO Modulation: Is It Decadally Predictable? *J. Climate*, 27(7):2667–2681.

Wittenberg, A., Rosati, A., Lau, N.-C., and Ploshay, J. (2006). GFDL's CM2 Global Coupled Climate Models. Part III: Tropical Pacific Climate and ENSO. *J.Climate*, 19(5):698–722.

Wittenberg, A. T., Rosati, A., Lau, N.-C., and Ploshay, J. (2004). GFDLs CM2 Global Coupled Climate Models. Part III: Tropical Pacific Climate and ENSO. *J.Climate*, 19:698–722.

Zebiak, S. and Cane, M. (1987). A Model El Nino-Southern Oscillation. *Month. Weath. Rev.*, 115:2262–2278.

Zeng, N., Neelin, J., and Chou, C. (2000). A Quasi-Equilibrium Tropical Circulation Model-Implementation and Simulation. *J. Atm. Sci.*, 57(11):1767–1796.

Zhang, C. (2005). Madden-Julian Oscillation. *Rev. Geophys.*, 43. RG2003, doi:10.1029/2004RG000158.

Zhang, C. and Gottschalck, J. (2002). SST Anomalies of ENSO and the Madden-Julian Oscillation in the Equatorial Pacific. *J. Climate*, 15(17):2429–2445.

Table Captions:

Table 1: Summary of model versions, their main features and comparison to GCMs.

Table 2: Model parameter definitions and nondimensional values.

Model	Crude Interannual	Crude Intraseasonal	TSS-GCM model	TSS-GCM model (Walker Circulation)	Conventional GCMs
Section	3.1	3.2	3.3	3.4	X
Complexity	Simple	Simple	Intermediate	Intermediate	Full Complexity
Formulation	Eq. 8, 9, 5-7 perturbed $\overline{a}$ and $u', v', q', \theta', a' = 0$	Eq. 11, 3, 5-7 $(\partial_t + d_a)a' = \Gamma q' \overline{a}$	Eq. 12, 3, 5-7 reference model	Eq. 12, 3, 5-7 unbalanced sources $s^\theta \neq s^q$	X
Stochastic noise	multiplicative	additive	multiplicative	multiplicative	X
Parameters	dissipations $d_u, d_q, d_a, \lambda = (30\, day)^{-1}$, noise amplitude $\sigma_q = 0.4$				X
Recovered Features	ENSO	ENSO, some MJOs	ENSO, MJO	ENSO, MJO, Walker Circulation	all of them but with common biases
Strengths	prototype for simple models with stochastic wind bursts	simplified intraseasonal dynamics	realistic convection and wind bursts, $a' + \overline{a} > 0$,	realistic convection and wind bursts, $a' + \overline{a} > 0$,	Full complexity of the ocean and atmosphere
Weaknesses	Gaussian SSTs, no intraseasonal variability	Gaussian SSTs, no convective details, excessive westward propagations	Gaussian SSTs	Gaussian SSTs	Gaussian SSTs weak/absent MJO computationally costly

Table 1: Summary of model versions, their main features and comparison to GCMs.

Parameter	nondimensional value
c ratio of ocean/atmosphere phase speed	0.05
ϵ Froude number	0.1
$c_1 = c/\epsilon$	0.5
L_A equatorial belt length	8/3
L_O equatorial Pacific length	1.2
$\overline{H}$ convective heating rate factor	22
$\overline{Q}$ mean vertical moisture gradient	0.9
Γ convective growth/decay rate	1.66
α_q latent heating factor	0.2
γ wind stress coefficient	6.53
ζ latent heating exchange coefficient	8.7
η profile of thermocline feedback	$\eta(x) = 1.5 + (0.5\tanh(7.5(x - L_O/2))$
$d_a, d_q, d_\theta, \lambda$ atmosphere dissipations	0.11
σ_q moisture noise amplitude	0.4
s^q external moistening source	$s^q = 2.2(1 + 0.6\cos(2\pi x/L_A))$
s^θ external cooling source	$s^\theta = s^q$ except Walker circulation: $s^\theta = 2.2(1 + 0.6\cos(2\pi x/L_A - 0.1))$

Table 2: Model parameter definitions and nondimensional values.

Figure Captions:

Figure 1: (a) Sketch of the couplings between the intraseasonal atmosphere, interannual atmosphere, ocean and SST as well as convective noise in the TSS-GCM model. (b-c) Sketch of the couplings in the (b) crude interannual and (c) crude intraseasonal model versions.

Figure 2: Zonal profiles of external moisture source s^q (black, $K.day^{-1}$) and cooling source s^θ(red, $K.day^{-1}$) for (a) the TSS-GCM model, and (b) the TSS-GCM model with dynamic Walker circulation (in addition to $s^m = (s^q - \overline{Q}s^\theta)/(1-\overline{Q})$ in blue), around the equatorial belt as a function of zonal position x (1000 km). (c) Zonal profile of the thermocline feedback parameter $\eta(x)$ in the equatorial Pacific (nondimensional). (d) Equilibrium Gamma probability distribution for convective activity (nondimensional).

Figure 3: Solutions of the crude interannual model. Timeseries of (a) T_E the average of SSTs in the eastern half of Pacific (K) and of (b) interannual convective activity $\overline{H}\overline{a}$ ($K.day^{-1}$) at the western edge of the Pacific ($x = 0$). The red line in (b) is a 1-year moving average. (c-d) repeats the timeseries over a shorter period. (e-f): Hovmollers of interannual (e) zonal winds $\overline{u}$ ($m.s^{-1}$), (f) thermocline depth H (m) and (g) SST T (K) at the equator, as a function of zonal position and time (years).

Figure 4: Solutions of the crude intraseasonal model. Zonal wavenumber-frequency power spectra: for intraseasonal (a) zonal winds u' ($m.s^{-1}$), (b) convective activity $\overline{H}a'$ ($K.day^{-1}$), (d) potential temperature θ' (K) and (e) moisture q' (K) and taken at the equator, as a function of wavenumber (2π/40000km) and frequency (cpd). The contour levels are in the base-10 logarithm for the dimensional variables taken at the equator. The dots indicate the dispersion relations of the linearized intraseasonal atmosphere. (c) Power spectrum of u'_W the average of u' in the western half of the equatorial Pacific (blue, $m.s^{-1}$) and of (f) T_E the average of T in the eastern half (blue, K), in addition to their smoothed versions (red). The dashed line indicate the periods 30 and 90 days in all subplots.

Figure 5: Solutions of the crude intraseasonal model. Hovmollers of (a) the MJO data projection e_{MJO}, intraseasonal (b) zonal winds u' ($m.s^{-1}$), (c) potential temperature θ' (K) and (d)

moisture q' (K), as well as (e) interannual zonal winds $\overline{u}$ ($m.s^{-1}$), (f) thermocline depth H (m) and (g) SST T (K) at the equator, as a function of zonal position x (1000 km) and time (years). Red line indicates the western Pacific edge at $x = 0$. The hovmollers in (a-e) extend from -10 000 to 18 000 km (Indian and Pacific oceans) while the hovmollers in (f-h) extend from 0 to 18 000 km (Pacific ocean only).

Figure 6: Solutions of the complete TSS-GCM model. Hovmollers of (a) the MJO data projection e_{MJO} (nondimensional), (b) intraseasonal zonal winds u' ($m.s^{-1}$), (c) total zonal winds $\overline{u} + u'$ ($m.s^{-1}$), (d) total convective activity $\overline{H}(\overline{a} + a')$ ($K.day^{-1}$ with values above $1\,K.day^{-1}$ not contoured), as well as (e) interannual convective activity $\overline{H}\overline{a}$ ($K.day^{-1}$), (f) interannual zonal winds $\overline{u}$ ($m.s^{-1}$), (f) thermocline depth H (m) and (g) SST T (K), at the equator, as a function of zonal position x (1000 km) and time (years). Red line indicates the western Pacific edge at $x = 0$. The hovmollers in (a-e) extend from -10 000 to 18 000 km (Indian and Pacific oceans) while the hovmollers in (f-h) extend from 0 to 18 000 km (Pacific ocean only).

Figure 7: Solutions of the complete TSS-GCM model. Timeseries of (a) T_E the average of SSTs in the eastern half of Pacific (K). (b) repeats the timeserie over a shorter period. (c-g): Hovmollers of (c) a 1-year running mean of $|e_{MJO}|$ the magnitude of the MJO data projection e_{MJO}, (d) interannual convective activity $\overline{H}\overline{a}$ ($K.day^{-1}$), (e) zonal winds $\overline{u}$ ($m.s^{-1}$), (f) thermocline depth H (m) and (g) SST T (K) at the equator, as a function of zonal position and time (years).

Figure 8: Solutions of the complete TSS-GCM model. Lagged regressions on T_E the average of SST in the eastern half of Pacific of (a) the MJO data projection e_{MJO} and (b) its magnitude $|e_{MJO}|$ (K^{-1}), (c) intraseasonal winds u' and (d) their magnitude $|u'|$ ($m.s^{-1}/K$), (e) interannual winds $\overline{u}$ ($m.s^{-1}/K$), (f) thermocline depth H (m/K) and (g) SST T (K/K), as a function of zonal position x (1000 km) and lag (years, positive for T_E leading). Red line indicates the western Pacific edge at $x = 0$.

Figure 9: Solutions of the complete TSS-GCM model. Zonal wavenumber-frequency power spectra: for intraseasonal (a) zonal winds u' ($m.s^{-1}$), (b) convective activity a' ($K.day^{-1}$), (e) potential temperature θ' (K) and (f) moisture q' (K) at the equator, as a function of wavenumber ($2\pi/40000$km) and frequency (cpd). The contour levels are in the base-10 logarithm for the dimen-

sional variables taken at the equator. The dots indicate the dispersion relations of the linearized intraseasonal atmosphere. (c,g) Power spectrum of (c) u'_W the average of u' in the western half of the equatorial Pacific $(m.s^{-1})$ and (g) of T_E the average of T in the eastern half (K). The dashed black lines indicate the periods 30 and 90 days in all subplots. (d) Probability density function of total convective activity $\overline{H}(\overline{a}+a')$ at the warm pool center/western Pacific edge $x=0$ $(K.day^{-1})$. Red dashed line in (d) indicates the corresponding equilibrium Gamma distribution from Eq. 10 for $E_q=0$. (h) Probability density function of T_E (K). Red dashed line in (h) is a Gaussian fit.

Figure 10: Solutions of the TSS-GCM model with dynamic Walker circulation. (a) Contours of time-averaged interannual convective activity $\overline{H}\overline{a}$ $(K.day^{-1})$e, as a function of zonal position (1000km) and height (km) in the equatorial Pacific. Arrows indicate time-averaged interannual zonal and vertical wind speed. (b-d). Zonal profiles of time-averaged (b) interannual zonal winds$\overline{u}$ $(m.s^{-1})$, (c) thermocline depth H (m) and (d) SST T (K) at the equator.

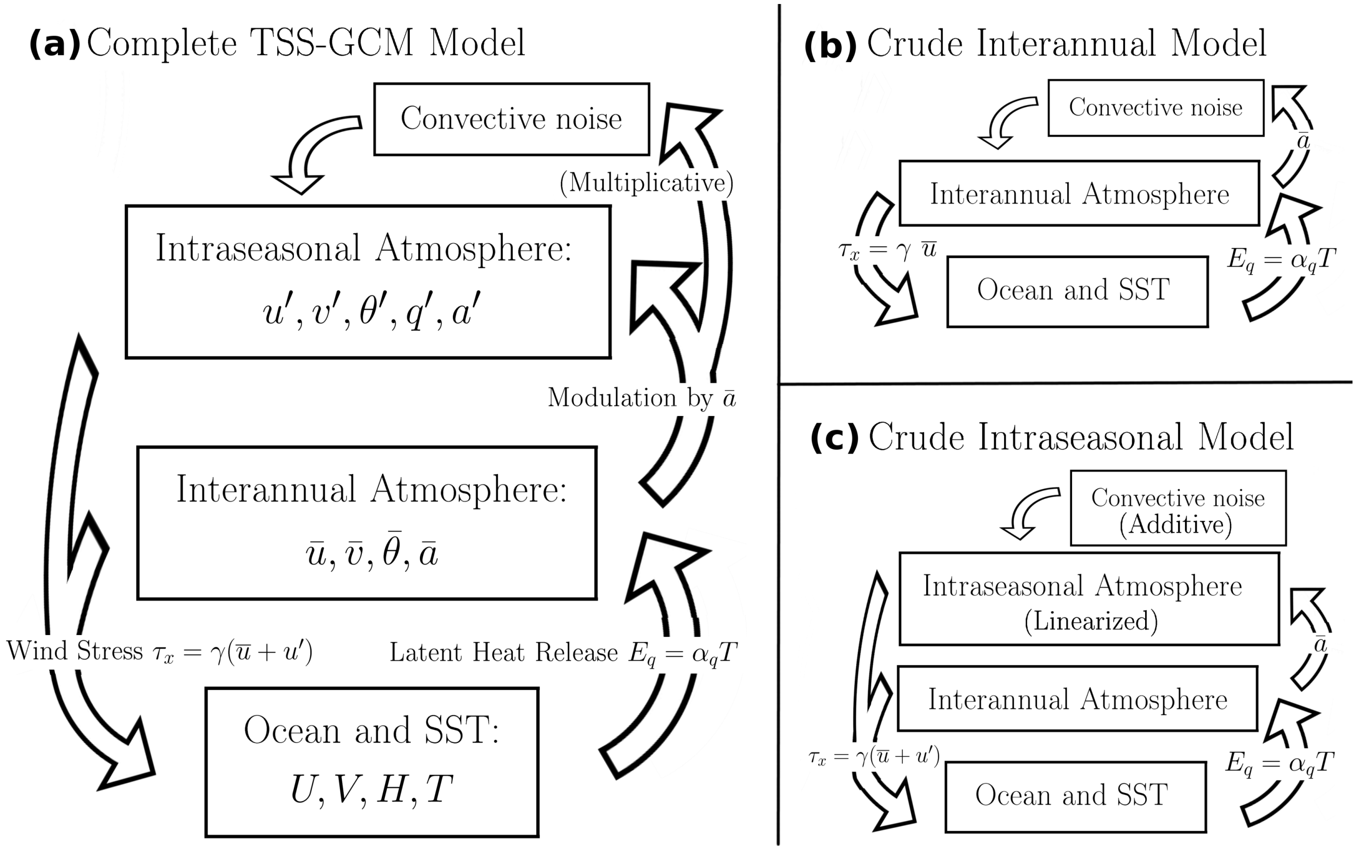

Figure 1: (a) Sketch of the couplings between the intraseasonal atmosphere, interannual atmosphere, ocean and SST as well as convective noise in the TSS-GCM model. (b-c) Sketch of the couplings in the (b) crude interannual and (c) crude intraseasonal model versions.

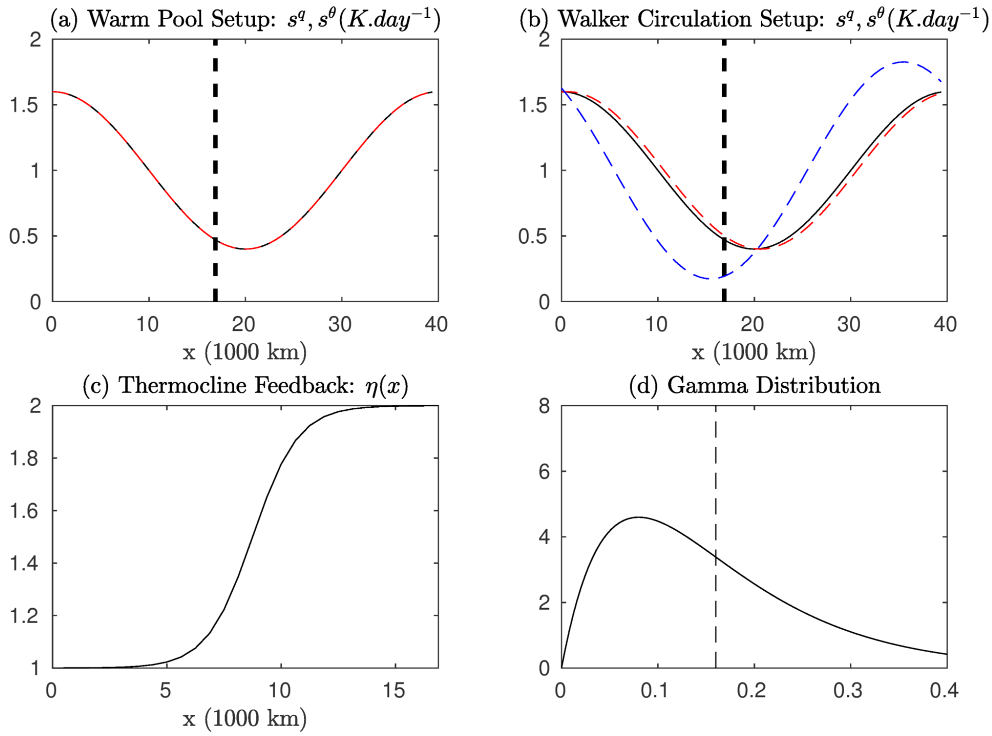

Figure 2: Zonal profiles of external moisture source s^q (black, $K.day^{-1}$) and cooling source s^θ(red, $K.day^{-1}$) for (a) the TSS-GCM model, and (b) the TSS-GCM model with dynamic Walker circulation (in addition to $s^m = (s^q - \overline{Q}s^\theta)/(1-\overline{Q})$ in blue), around the equatorial belt as a function of zonal position x (1000 km). (c) Zonal profile of the thermocline feedback parameter $\eta(x)$ in the equatorial Pacific (nondimensional). (d) Equilibrium Gamma probability distribution for convective activity (nondimensional).

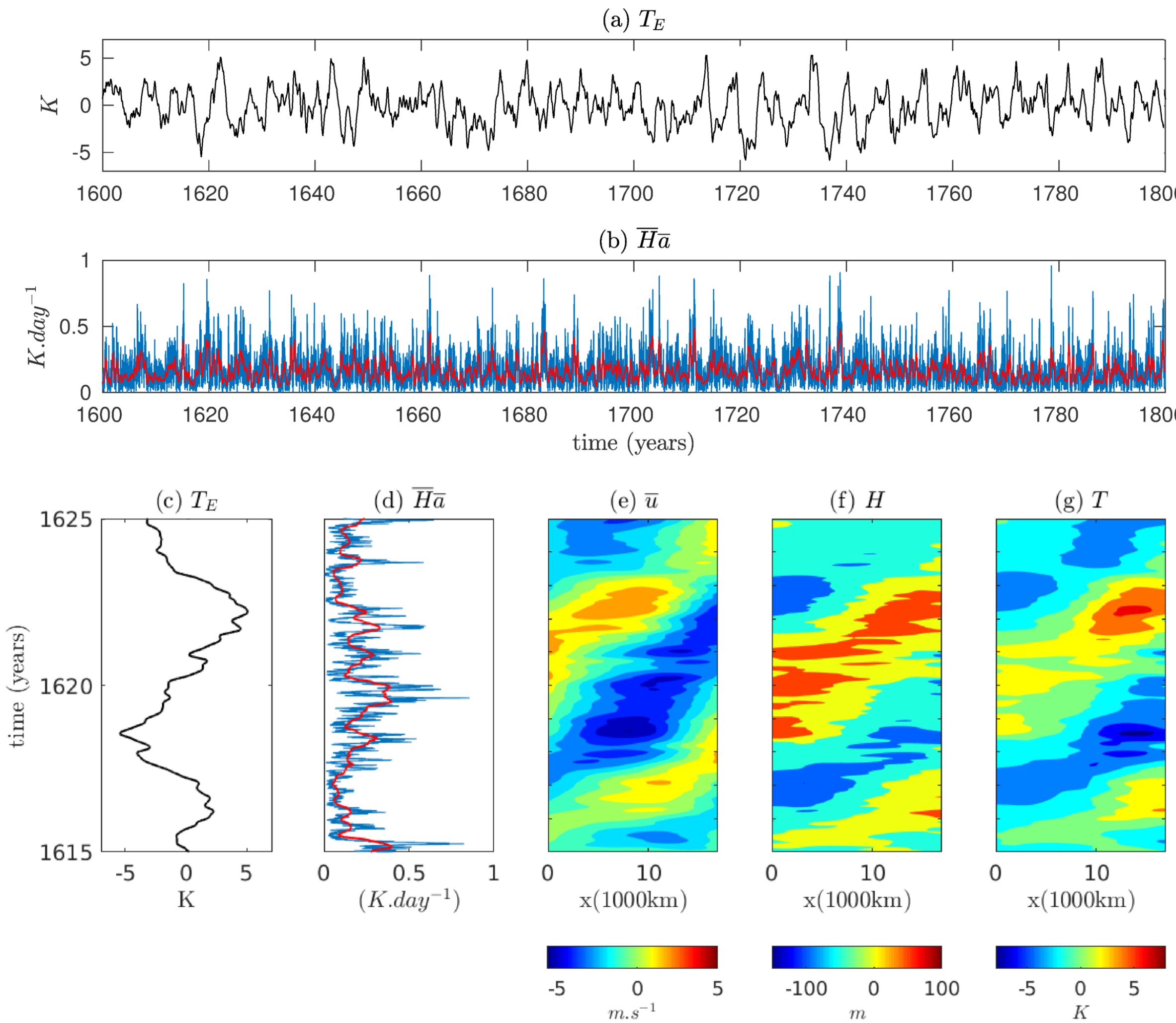

Figure 3: Solutions of the crude interannual model. Timeseries of (a) T_E the average of SSTs in the eastern half of Pacific (K) and of (b) interannual convective activity $\overline{H}\overline{a}$ ($K.day^{-1}$) at the western edge of the Pacific ($x = 0$). The red line in (b) is a 1-year moving average. (c-d) repeats the timeseries over a shorter period. (e-f): Hovmollers of interannual (e) zonal winds $\overline{u}$ ($m.s^{-1}$), (f) thermocline depth H (m) and (g) SST T (K) at the equator, as a function of zonal position and time (years).

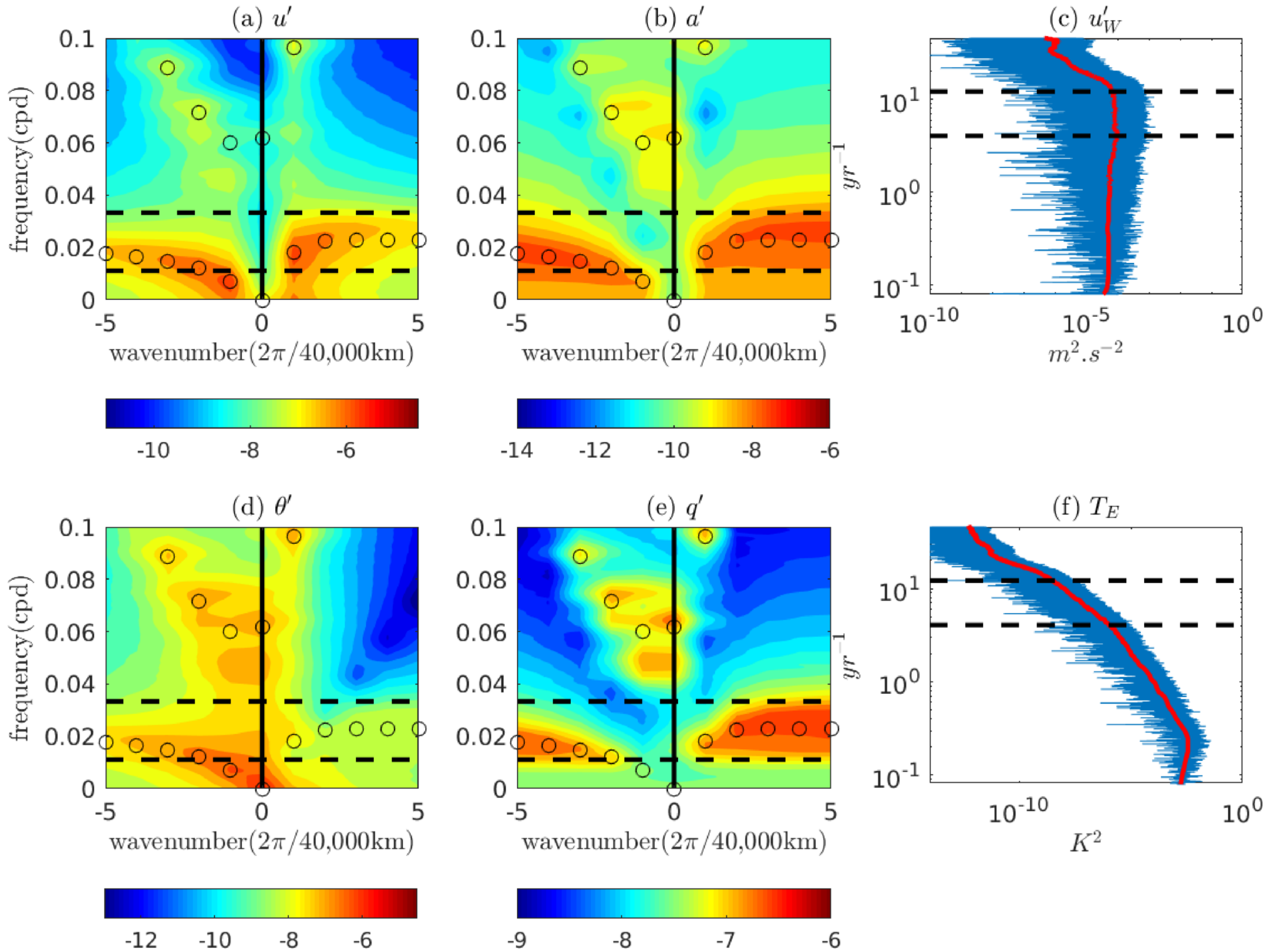

Figure 4: Solutions of the crude intraseasonal model. Zonal wavenumber-frequency power spectra: for intraseasonal (a) zonal winds u' ($m.s^{-1}$), (b) convective activity $\overline{H}a'$ ($K.day^{-1}$), (d) potential temperature θ' (K) and (e) moisture q' (K) and taken at the equator, as a function of wavenumber ($2\pi/40000$km) and frequency (cpd). The contour levels are in the base-10 logarithm for the dimensional variables taken at the equator. The dots indicate the dispersion relations of the linearized intraseasonal atmosphere. (c) Power spectrum of u'_W the average of u' in the western half of the equatorial Pacific (blue, $m.s^{-1}$) and of (f) T_E the average of T in the eastern half (blue, K), in addition to their smoothed versions (red). The dashed line indicate the periods 30 and 90 days in all subplots.

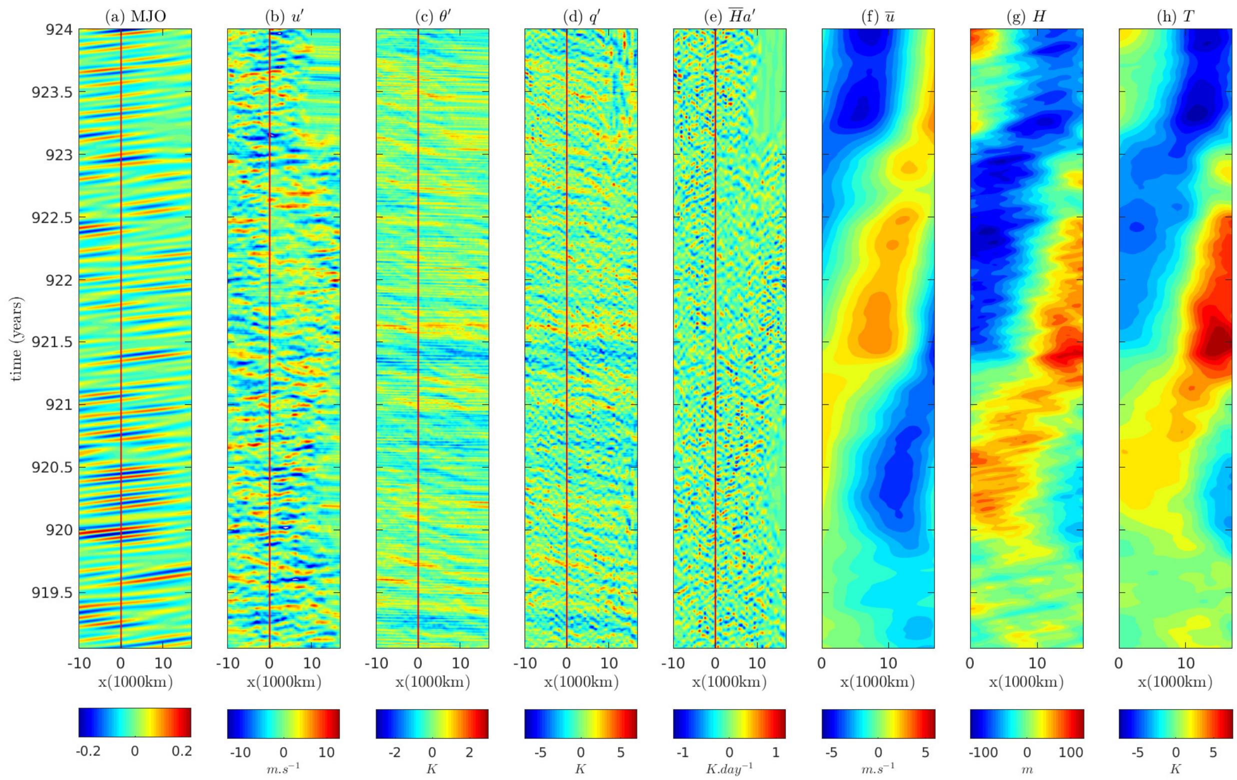

Figure 5: Solutions of the crude intraseasonal model. Hovmollers of (a) the MJO data projection e_{MJO}, intraseasonal (b) zonal winds u' ($m.s^{-1}$), (c) potential temperature θ' (K) and (d) moisture q' (K), as well as (e) interannual zonal winds $\overline{u}$ ($m.s^{-1}$), (f) thermocline depth H (m) and (g) SST T (K) at the equator, as a function of zonal position x (1000 km) and time (years). Red line indicates the western Pacific edge at $x = 0$. The hovmollers in (a-e) extend from -10 000 to 18 000 km (Indian and Pacific oceans) while the hovmollers in (f-h) extend from 0 to 18 000 km (Pacific ocean only).

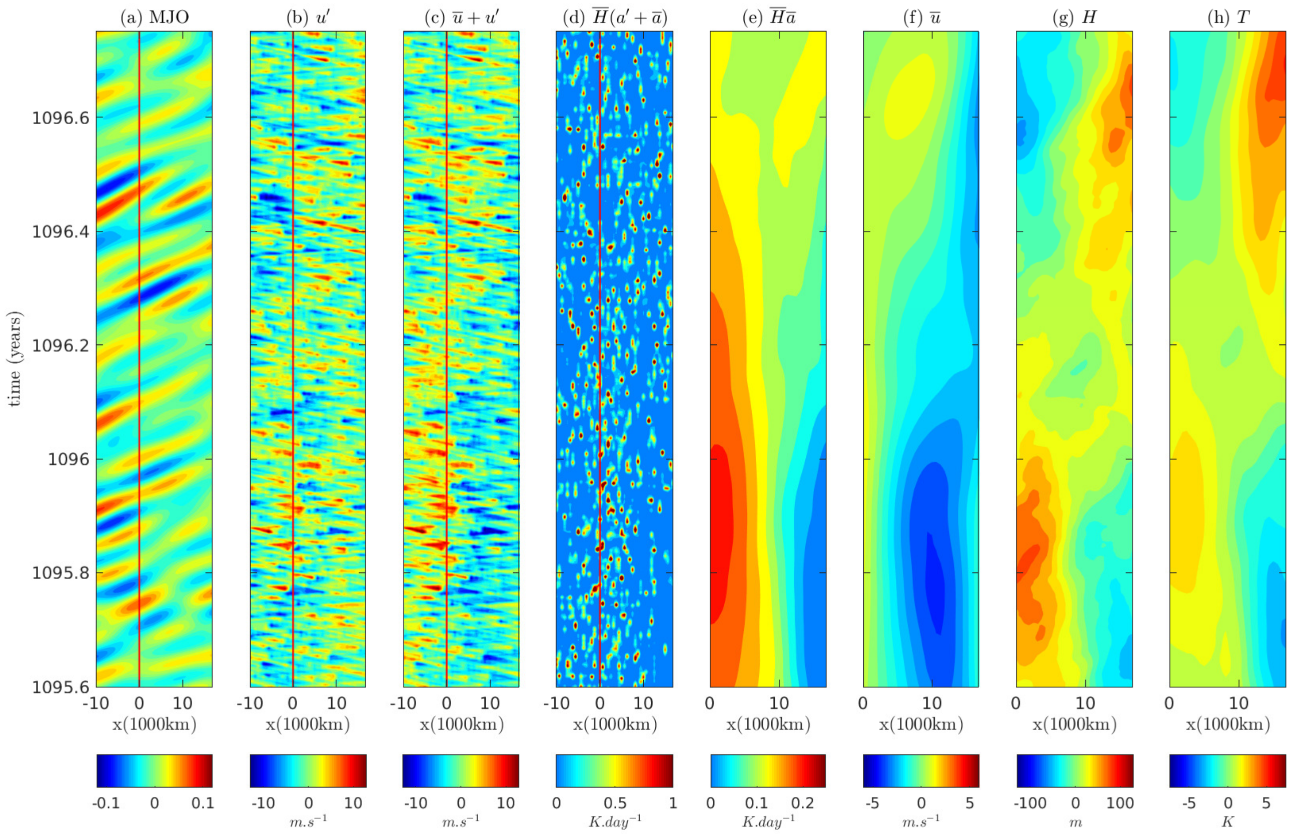

Figure 6: Solutions of the complete TSS-GCM model. Hovmollers of (a) the MJO data projection e_{MJO} (nondimensional), (b) intraseasonal zonal winds u' ($m.s^{-1}$), (c) total zonal winds $\overline{u}+u'$ ($m.s^{-1}$), (d) total convective activity $\overline{H}(\overline{a}+a')$ ($K.day^{-1}$ with values above $1\,K.day^{-1}$ not contoured), as well as (e) interannual convective activity $\overline{H}\overline{a}$ ($K.day^{-1}$), (f) interannual zonal winds $\overline{u}$ ($m.s^{-1}$), (f) thermocline depth H (m) and (g) SST T (K), at the equator, as a function of zonal position x (1000 km) and time (years). Red line indicates the western Pacific edge at $x = 0$. The hovmollers in (a-e) extend from -10 000 to 18 000 km (Indian and Pacific oceans) while the hovmollers in (f-h) extend from 0 to 18 000 km (Pacific ocean only).

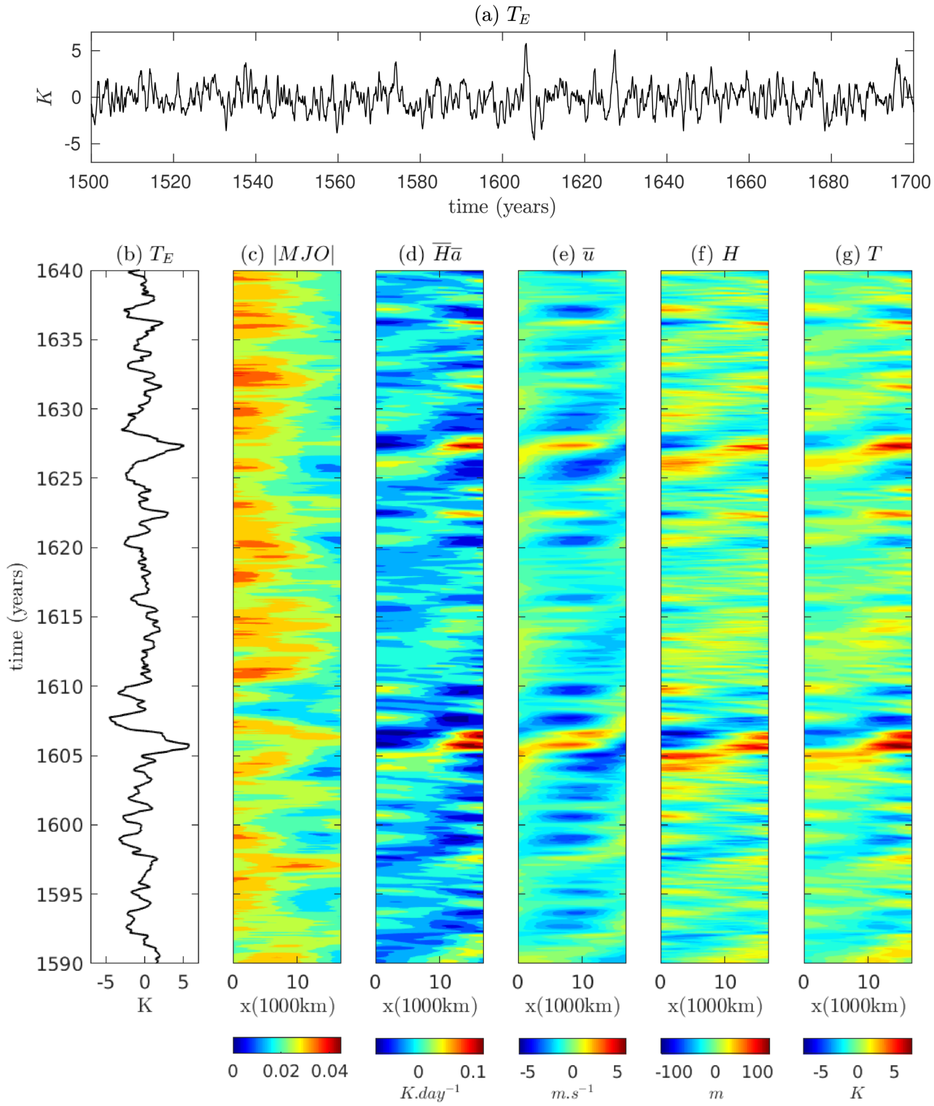

Figure 7: Solutions of the complete TSS-GCM model. Timeseries of (a) T_E the average of SSTs in the eastern half of Pacific (K). (b) repeats the timeserie over a shorter period. (c-g): Hovmollers of (c) a 1-year running mean of $|e_{MJO}|$ the magnitude of the MJO data projection e_{MJO}, (d) interannual convective activity $\overline{H}\overline{a}$ ($K.day^{-1}$), (e) zonal winds $\overline{u}$ ($m.s^{-1}$), (f) thermocline depth H (m) and (g) SST T (K) at the equator, as a function of zonal position and time (years).

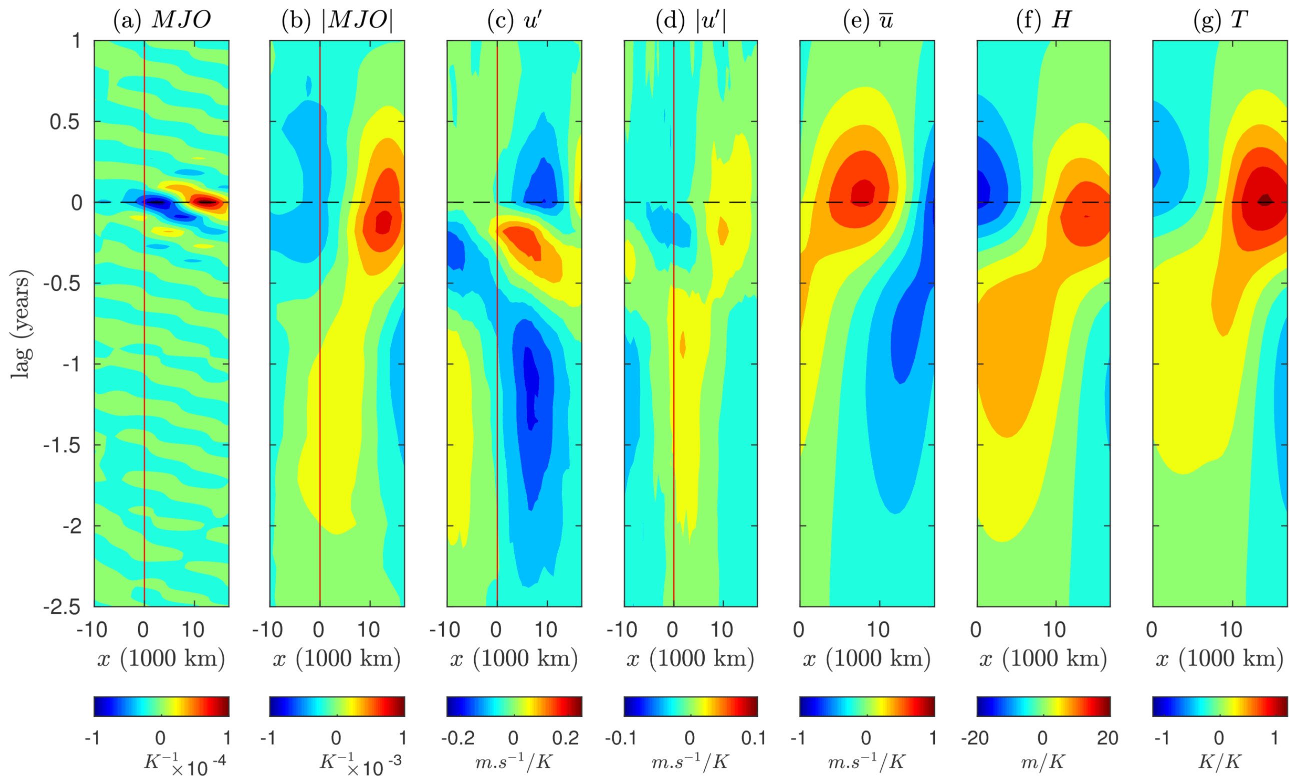

Figure 8: Solutions of the complete TSS-GCM model. Lagged regressions on T_E the average of SST in the eastern half of Pacific of (a) the MJO data projection e_{MJO} and (b) its magnitude $|e_{MJO}|$ (K^{-1}), (c) intraseasonal winds u' and (d) their magnitude $|u'|$ ($m.s^{-1}/K$), (e) interannual winds $\overline{u}$ ($m.s^{-1}/K$), (f) thermocline depth H (m/K) and (g) SST T (K/K), as a function of zonal position x (1000 km) and lag (years, positive for T_E leading). Red line indicates the western Pacific edge at $x = 0$.

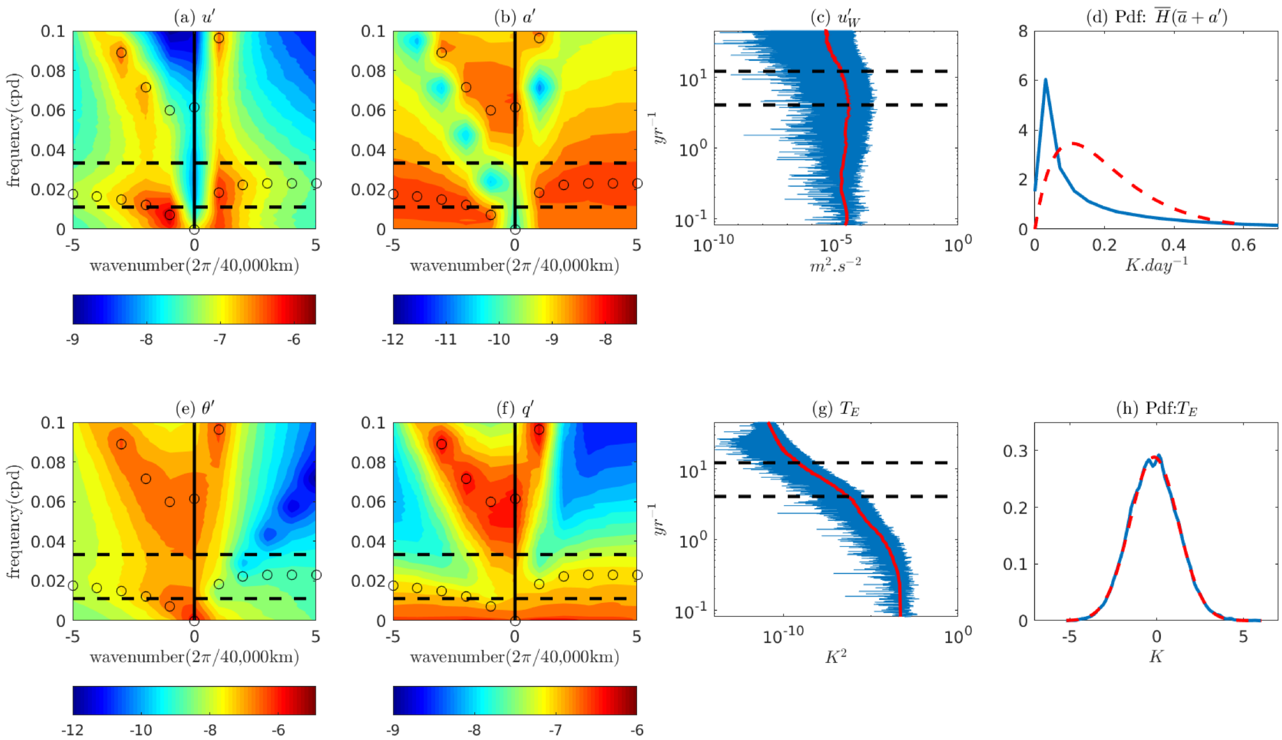

Figure 9: Solutions of the complete TSS-GCM model. Zonal wavenumber-frequency power spectra: for intraseasonal (a) zonal winds u' ($m.s^{-1}$), (b) convective activity a' ($K.day^{-1}$), (e) potential temperature θ' (K) and (f) moisture q' (K) at the equator, as a function of wavenumber (2π/40000km) and frequency (cpd). The contour levels are in the base-10 logarithm for the dimensional variables taken at the equator. The dots indicate the dispersion relations of the linearized intraseasonal atmosphere. (c,g) Power spectrum of (c) u'_W the average of u' in the western half of the equatorial Pacific ($m.s^{-1}$) and (g) of T_E the average of T in the eastern half (K). The dashed black lines indicate the periods 30 and 90 days in all subplots. (d) Probability density function of total convective activity $\overline{H}(\overline{a}+a')$ at the warm pool center/western Pacific edge $x=0$ ($K.day^{-1}$). Red dashed line in (d) indicates the corresponding equilibrium Gamma distribution from Eq. 10 for $E_q=0$. (h) Probability density function of T_E (K). Red dashed line in (h) is a Gaussian fit.

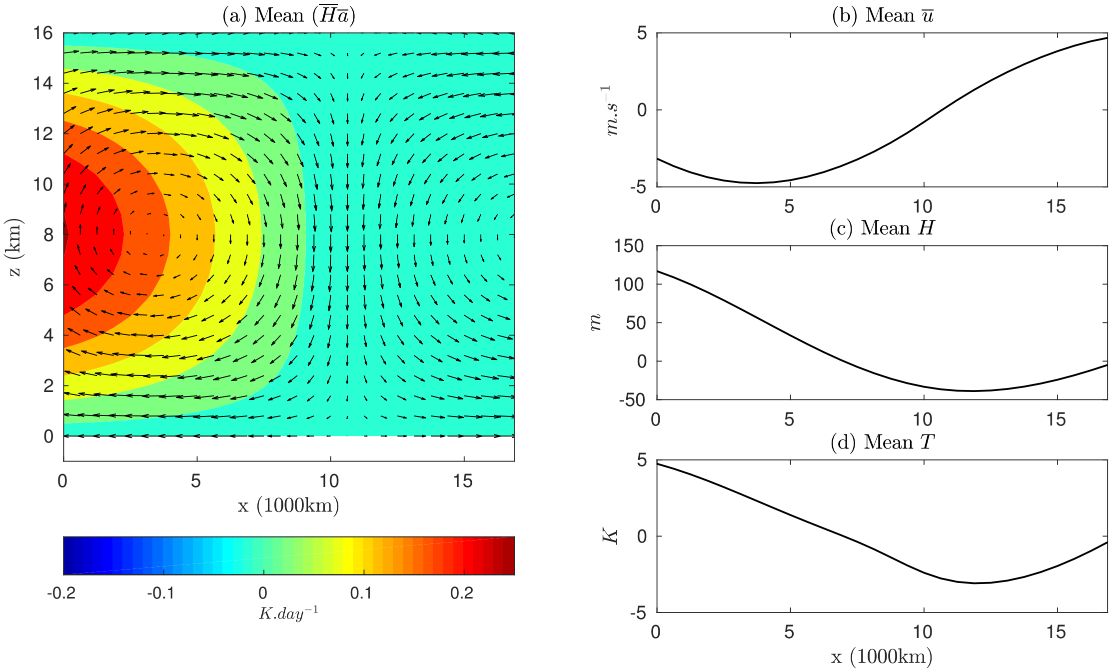

Figure 10: Solutions of the TSS-GCM model with dynamic Walker circulation. (a) Contours of time-averaged interannual convective activity $\overline{H}\overline{a}$ $(K.day^{-1})$e, as a function of zonal position (1000km) and height (km) in the equatorial Pacific. Arrows indicate time-averaged interannual zonal and vertical wind speed. (b-d). Zonal profiles of time-averaged (b) interannual zonal winds$\overline{u}$ $(m.s^{-1})$, (c) thermocline depth H (m) and (d) SST T (K) at the equator.